

Chapter 6

Sparse Array Design for Direction Finding using Deep Learning¹

Kumar Vijay Mishra,^{1*} Ahmet M. Elbir,² and Koichi Ichige³

¹*Computational and Information Sciences Directorate (CISD), United States DEVCOM Army Research Laboratory, 20783, Adelphi, Maryland, USA*

²*Interdisciplinary Centre for Security, Reliability and Trust (SnT), University of Luxembourg, 1855, Av. John F. Kennedy, Luxembourg*

³*Department of Electrical and Computer Engineering, Yokohama National University, 240-8501, Yokohama, Japan*

*Corresponding Author: Kumar Vijay Mishra; kvm@ieee.org

Abstract: In the past few years, deep learning (DL) techniques have been introduced for designing sparse arrays. These methods offer the advantages of feature engineering and low prediction-stage complexity, which is helpful in tackling the combinatorial search inherent to finding a sparse array. In this chapter, we provide a synopsis of several direction finding applications of DL-based sparse arrays. We begin by examining supervised and transfer learning techniques that have applications in selecting sparse arrays for a cognitive radar application. Here, we also discuss the use of meta-heuristic learning algorithms such as simulated annealing for the case of designing two-dimensional sparse arrays. Next, we consider DL-based antenna selection for wireless communications, wherein sparse array problem may also be combined with channel estimation, beamforming, or localization. Finally, we provide an example of deep sparse array technique for integrated sensing and communications (ISAC) application, wherein a trade-off of radar and communications performance makes ISAC sparse array problem very challenging. For each setting, we illustrate the performance of model-based optimization and DL techniques through several numerical experiments. We discuss additional considerations required to ensure robustness of DL-based algorithms against various imperfections in array data.

Keywords: Antenna selection, direction finding, beamforming, deep learning, sparse arrays.

6.1. Introduction

Phased sensor arrays have become widely prevalent in various applications such as radar, sonar, communications, acoustics, sounding, and ultrasound [1, 2, 3, 4]. They allow electronic beam steering without requiring any mechanical motion, providing high spatial selectivity and the ability to reject interference. However, according to the Nyquist-Shannon theorem, the array must allow for at least two signal samples in a single spatial period, which is the same as the array's operating wavelength [5]. Otherwise, *spatial aliasing*

¹K. V. M. acknowledges support from the National Academies of Sciences, Engineering, and Medicine via Army Research Laboratory Harry Diamond Distinguished Fellowship.

occurs resulting in multiple main-lobes appearing in the beampattern, which reduces the directivity and affects the accuracy of estimating bearings or directions-of-arrival (DoAs) of unknown sources or targets [6]. To avoid this, conventional phased sensor arrays employ a uniform linear array (ULA), wherein sensors must be separated *at most* by half-wavelength spacing. However, as the number of sensors increases, the associated complexity, size, and cost of arrays become unacceptable. As a result, there is growing interest in thinned or sparse sensor arrays, which offer significantly reduced hardware [7, 8, 9].

Uniformly removing sensors from a ULA produces *grating lobes* or copies of the main lobe. This effect can be suppressed by removal of sensors at random locations giving rise to *thinned* or *sparse* arrays [10, 11]. However, randomly thinned arrays are accompanied by increased sidelobe levels, which hampers direction finding. Further, the number of elements in an array determines its degrees-of-freedom (DoFs) or the number of sources whose bearings can be determined by the sensor array. A full or filled sensor array with N elements has more DoFs than a sparse array with only $\mathcal{O}(\sqrt{N})$ sensors [8, 1]. But, with suitable parameter recovery algorithms [12, 9, 13, 14], sparse arrays have been shown to exhibit negligible performance degradation and reduced mutual coupling in direction finding [15, 16, 17] and spatial filtering [18]. Most of these algorithms employ sparse recovery techniques, including compressed sensing (CS) [19].

6.1.1. Prior Art and Historical Notes

Sparse array literature could be traced back to the seminal works of Y. T. Lo [10, 11], who studied the probabilistic properties (e.g. the probability of the array pattern crossing a specified sidelobe level) of random arrays. Other studies published around the same time [20, 21, 22] focused on approximating the analytic expressions of desired antenna patterns with few nonuniformly-spaced elements but these were optimal only for smaller arrays. This was followed by sparse array designs using vastly different procedures such as dynamic programming [23], iterative least squares [24], nonlinear optimization [25], genetic algorithms [8], and simulated annealing (SA) [26]. These techniques are usually limited by slow speed of optimization, high sidelobes, non-optimality for large arrays, and high dependence of final element placement based on the choices made in previous iterations.

Other geometries of non-uniformly-spaced sparse arrays that have low sidelobes were also proposed; see, e.g., [27] for an overview, and references therein. For example, [28] describes a fractal-based quasi-random array that combines properties of both random and periodic arrays such that its peak sidelobe level (PSL) is lower than a purely random array. A space-tapered array [29, 30] places antennas with increasing inter-element spacing as one moves away from the aperture's center thereby achieving low PSL but higher integrated sidelobe levels (ISL) than random arrays.

A sparse array is hole-free or *restricted* if its difference coarray is a ULA, otherwise it is a *general* array. A sparse array with N sensors and the aperture defined by the integer grid $[-M, M]$ may also be characterized by its *redundancy ratio* $R = N(N - 1)/(2M) \geq 1$, which is the number of pairs of antennas divided by the aperture [31]. Using this metric, zero redundancy arrays (ZRAs) [32], minimum redundancy arrays

(MRAs) [31], and low redundancy arrays (LRAs) [33] were proposed. These minimize spatial aliasing while maintaining a reasonably constant ISL. The ZRAs have $R = 1$ but they exist for only $N \leq 4$ [34]. The MRAs, which achieve the lowest R , select the missing elements such that the resulting sparse array has all possible inter-element spacings of the full array. Leech's bounds [35] for MRAs stipulate $1.217 \leq R \leq 1.674$ for $N \rightarrow \infty$. Optimal solutions for $N \leq 11$ were provided in [35] and, using exhaustive computer-aided search, expanded later to $N \leq 26$ [36]. For larger N , the procedure becomes increasingly complex [37] and there have been efforts to meet the Leech's lower bound through LRAs [33]. These problems have led to the popularity of more structured sparse designs such as co-prime arrays [38, 39, 40]. While these configurations provide a closed form of sensor positions and offer enhanced DoFs for parameter estimation, they are not applicable to arbitrary number of antenna elements.

6.1.2. Learning-Based Approaches

In general, searching for an optimal sparse sensor array is a combinatorial problem [31], whose computational complexity increases with the number of sensors. Since a closed-form solution is difficult to come by, several sub-optimal (although mathematically tractable) solutions have been proposed [41, 16, 13, 42, 43, 44]. Recently, there has been a growing interest in utilizing learning-based approaches in sparse sensor communications [18, 45] and signal processing [46, 47].

Deep learning (DL) has been shown to offer better computational efficiency than a combinatorial search [18, 48]. DL has been extremely effective in addressing challenging problems such as speech recognition, visual object recognition, and language processing [49, 50]. It offers advantages such as low computational complexity while tackling optimization-based or combinatorial search problems, and the ability to generate new features from a limited set of features available in a training set [51, 49].

In a typical DL-based sparse array design (Fig. 6.1), the antenna array data is fed into the DL network, which yields the indices of the selected antennas at the output. To train the DL model, the input datasets vary and may comprise of the raw array output [18], covariance matrix [52] or the autocorrelation function [53] of the array data. The output layer of the model is usually a classification layer, wherein each class corresponds to a possible set of subarray indices. In some case, the output is a regression layer, whose values are either 0 or 1 indicating the (un)selected antennas [46].

The rest of the chapter is organized as follows: In the next section, we review general DL design procedures for sparse array design and direction-of-arrival (DoA) estimation. Then, Section 6.3) describes a major use case of this technique in cognitive radar, where a dynamic transmit antenna selection is required for the changing target environment. A DL-based approach is able to yield sparse (sub-)arrays in real-time for this application. When insufficient training data are available for a new antenna geometry, then Section 6.4 presents a transfer learning (TL) approach to utilize a trained network from a different antenna configuration. For planer or two-dimensional (2-D) large sparse arrays, usually a combination of SA and DL may be more appropriate, as detailed in Section 6.5. We then consider DL for sparse array applications in wireless commu-

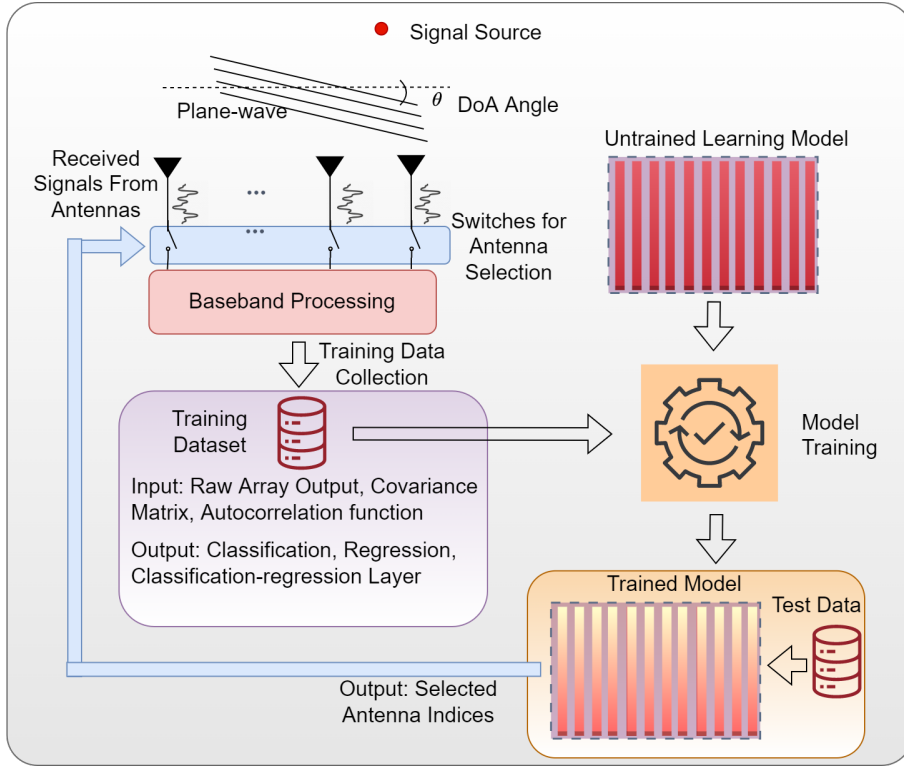


Figure 6.1: Illustration of DL-based antenna selection.

nications by combining antenna selection with massive multiple-input multiple-output (MIMO) beamforming (Section 6.6) and integrated sensing and communications (ISAC) [54] (Section 6.7). Finally, we summarize our key observations and unaddressed challenges in Section 6.8.

Notations: Throughout the chapter, we reserve boldface lowercase and uppercase letters for vectors and matrices, respectively. The i th element of a vector \mathbf{y} is $y(i)$ while the (i, j) th entry of the matrix \mathbf{Y} is $[\mathbf{Y}]_{i,j}$. We denote the transpose and Hermitian by $(\cdot)^T$ and $(\cdot)^H$, respectively. The functions $\angle \{\cdot\}$, $\Re \{\cdot\}$ and $\Im \{\cdot\}$ designate the phase, real and imaginary parts of a complex argument, respectively. The combination of selecting K terms out of M is denoted by $\binom{M}{K} = \frac{M!}{K!(M-K)!}$. The Hadamard (point-wise) product is written as \odot . The functions $\mathbb{E} \{\cdot\}$ and \max give the statistical expectation and maximum value of the argument, respectively. The notation $x \sim \mathbf{u}\{[u_l, u_u]\}$ means a random variable drawn from the uniform distribution over $[u_l, u_u]$ and $x \sim \mathcal{CN}(\mu_x, \sigma_x^2)$ represents the complex normal distribution with mean μ_x and variance σ_x^2 .

6.2. General Design Procedures

DL-based design for sparse arrays comprise diverse procedures that differ in performance criteria, performance metrics and input/output data types for the learning model (Fig. 6.2).

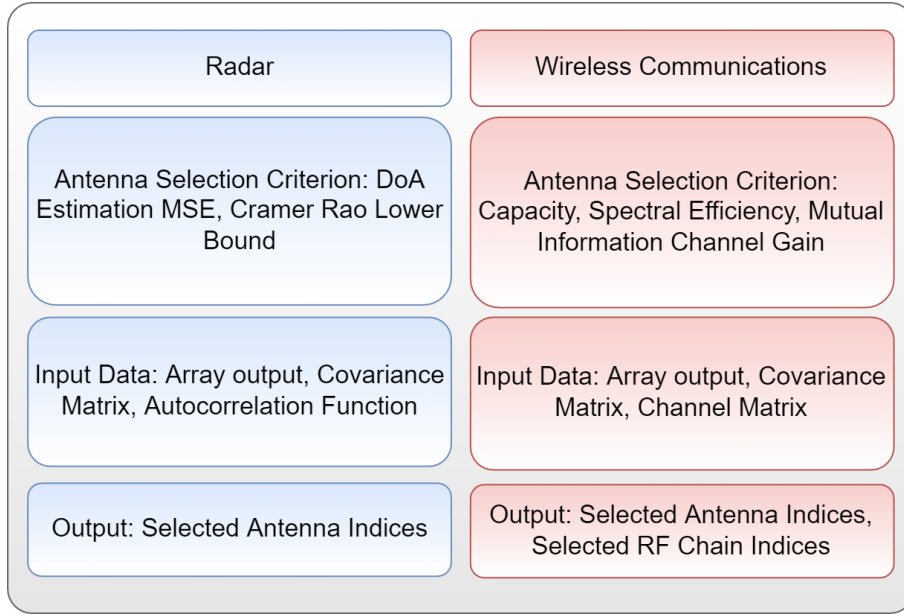


Figure 6.2: Design procedures for DL-based antenna selection for the applications in radar and wireless communications.

For instance, in wireless communications, sparse arrays manifest as antenna selection problem to reduce the complexity of common communications tasks such as channel estimation, beamforming, resource allocation, and user localization [42, 55]. On the other hand, other sparse geometries (e.g., coprime and nested arrays) are used to improve the DoF of the overall system, especially in radar applications [38, 56, 16, 57].

The data-driven nature of DL allows us to employ a ground-truth dataset to find the best sparse array configuration. While some methods use DL, others choose simpler machine learning methods with shallow learning models, e.g. simple feed-forward neural networks [49, 58]. Although defining the optimum sparse array search as a binary segmentation problem is theoretically possible, current DL-based models do not consider the problem as a multilabel classification task. We summarize some major approaches below.

Antenna Selection Setups The potential array setups are translated into labels and a classification model is trained to find the optimum array structure. If the array setups are required to be in a specific configuration, e.g., minimum hole array (MHA), MRA, or nested arrays, either a constraint is added to the loss function to guarantee a desired architecture, or the set of possible sparse array designs is reduced to a set of sparse arrays following further constraints by a searching algorithm beforehand. The learned sparse array can be tested with any of the DoA estimation methods. In [46], a convolutional neural network (CNN) is used on a dataset composed of an $N \times N \times 3$ matrix representing real, imaginary, and angle components of a complex covariance matrix as input and each possible subarray for a given ULA as a class label as output. The problem is defined as the minimization of the Cramér-Rao bound (CRB), which limits the minimum variance of the correlation matrix in the DoA estimation problem. The learning model returns an appropriate subarray for individual received data, and thus works as a cognitive antenna

array. The model is intended to be used as a cognitive selector, meaning that the model is used in real-time to determine the best sparse array to use in analysis by reading the incoming signal and changing the selected sparse array at a given period.

The model in [46] returns suboptimal 1-D arrays. The final arrays include elements at the end of the ULA grid without including surrounding elements. This issue results in coarray having many holes, causing high peak sidelobes and reducing the performance. To tackle this problem, [59] restricted the available antenna subarrays to the ones with minimal hole setup. Here, k -essential property is used to eliminate sensors from a ULA, which shows whether the coarray changes from the ULA or not when the elements are removed. The M - N sensors that are not essential can thus be discarded. The results show that the estimated subarrays provide a better beampattern with suppressed peak side lobes and a narrower main lobe. Estimated sparse arrays of this model also show much lower root mean-squared error (RMSE) values compared to [46].

Among model-based learning approaches, [60] performed antenna selection from a CRB minimization problem defined as a weight vector selection that gives the minimum CRB for a given number of non-zero weights at the output of the learning model. To make the original problem tractable, Dinkelbach approximation was used and solved by applying *advanced gradient descent* (AdaGrad) algorithm on a loss function.

DoA Estimation Setups Some DL-based DoA estimation models include sparsity of the array design in their architecture in order to exploit the advantages of the sparse arrays. Model-based methods require the covariance matrix to be full, which is impossible in sparse array structures. DL-based methods specifically designed to work with sparse arrays are proven to be powerful enough to overcome this issue and learn an accurate mapping between sparse covariance matrices and arrival angles [46, 61]. These models can also utilize the coarray principle and detect more signal sources than the number of sensors in the sparse array.

In [62], a two-layer CNN was trained to estimate DoA angles. The array structure is a combination of different subarrays with the same number of elements. The position between different subarrays is assumed to be unknown while only the relative position of elements in each subarray is known. The model input is the fusion of the estimated covariance matrix of each subarray created with an element-wise sum and vectorization while the output yields the DoA angles. It is shown that the learning model can learn to detect more signal sources than the number of elements thanks to employing sparse arrays.

A deep CNN model called RFDOA-Net was designed in [63] to estimate the DoA angles for unmanned aerial vehicles (UAVs) with a complex architecture using multi-scale feature processing. The learning model was trained with a synthetic dataset with different signal-to-noise-ratio (SNR) values over a 5-element sparse coarray and used raw antenna inputs converted into an input matrix of antenna elements with respect to snapshots. The output data was a vector of the probability distribution of the DoA angles.

In [53], CNN-based DoA estimation was studied with nested arrays. The input of the CNN was a proxy spectrum obtained from the autocorrelation of the nested array output. The output layer of the CNN included the angular spectra, of which the highest

peaks corresponds to the source directions [52].

Some models are designed to capture both azimuth and elevation angles with a 3-D sparse array structure. In [64], CNN was applied on the 2-D readings of a coprime circular conformal (stacked array arrangement) microphone array (C3MA) to estimate the DoA angles of audio signals. The model took the cross-correlation value of individual microphones as input while the output yields the 2-D DoA angles.

6.3. Cognitive Sparse Array Design for DoA Estimation

We now examine a DL-based antenna selection procedure in detail for a cognitive radar application. The DL techniques directly fit this setting because the antenna selection problem can be considered as a classification problem, wherein each subarray designates a class. We leverage DL to consider a relatively large scale of the selection problem wherein the feature maps can be extracted to train the network for different array geometries. Unlike random array thinning where a fixed subarray is used for all scans, we select a new subarray based on the received data. In contrast to [44, 65], we also assume that the target DoA angle is unknown while choosing the array elements.

We employ a CNN, whose input data are the covariance samples of the received array signal. The CNN architecture models the selection of K best antennas out of M as a classification problem wherein each class denotes an antenna subarray. In order to create the training data, we choose those subarrays which estimate DoA with the lowest minimal bound on the mean-squared-error (MSE) so that the selected subarray can yield the best performance for the given scenario. We consider minimization of CRB as the performance benchmark in generating training sets for 1-D ULA and 2-D geometries such as uniform circular arrays (UCA) and randomly deployed arrays (RDA). For ULAs, the network is also trained with data obtained by minimizing Bayesian bounds such as the Bobrovsky-Zakai bound (BZB) and Weiss-Weinstein bound (WWB) on DoA [66] because these bounds provide better estimates of MSE at low SNRs. In particular, BZB-based selection has been shown to have the ability to control the sidelobes and avoid ambiguity in DoA estimation [67, 68].

6.3.1. Signal Model

Consider a phased array antenna with M elements where each element transmits a pulsed waveform $s(t_i)$ towards a Swerling Case 1 point target for $i = 1, \dots, T$, where T is the number of data snapshots. Since we are interested only in DoA recovery, the range and Doppler measurements are not considered and target's complex reflectivity is set to unity. Assumption of a Swerling I model implies that the target parameters remain constant for the duration of the scan. We characterize the target through its DoA $\Theta = (\theta, \phi)$ where θ and ϕ denote, respectively, the elevation and the azimuth angles with respect to the radar. The radar's pulse repetition interval and operating wavelength are, respectively, T_s and $\lambda = c_0/f_0$, where $c_0 = 3 \times 10^8 \text{ ms}^{-1}$ is the speed of light and $f_0 = \omega_0/2\pi$ is the carrier frequency.

To further simplify the geometries, we suppose that the targets are far enough from the radar so that the received signal wavefronts are effectively planar over the array. The array receives a narrowband signal reflected from a target located in the far-field of the array at Θ . Then, the output of the sensor array is [69]

$$\mathbf{y}(t_i) = \mathbf{a}(\Theta)s(t_i) + \mathbf{n}(t_i), \quad 1 \leq i \leq T, \quad (6.1)$$

where T is the number of snapshots, $\mathbf{y}(t_i) = [y_1(t_i), \dots, y_M(t_i)]^T$ and $y_m(t_i)$ denotes the output of the m -th sensor for the i -th snapshot, $\mathbf{n}(t_i) = [n_1(t_i), \dots, n_M(t_i)]^T$ is the noise vector and $n_m(t_i)$ is zero-mean spatially and temporarily white Gaussian noise with variance σ_n^2 , $\mathbf{a}(\Theta) = [a_1(\Theta), \dots, a_M(\Theta)]^T$ is the $M \times 1$ steering vector. The m -th element of $\mathbf{a}(\Theta)$ is

$$a_m(\Theta) = \exp \left\{ -j \frac{2\pi}{\lambda} \mathbf{p}_m^T \mathbf{r}(\Theta) \right\}, \quad (6.2)$$

where $\mathbf{r}(\Theta)$ depends on the source direction as

$$\mathbf{r}(\Theta) = [\cos(\phi) \sin(\theta), \sin(\phi) \sin(\theta), \cos(\theta)]^T, \quad (6.3)$$

and $\mathbf{p}_m = [x_m, y_m, z_m]^T$ is the position of the m -th sensor in the Cartesian coordinate system. Expanding the inner product $\mathbf{p}_m^T \mathbf{r}(\Theta)$ in the array steering vector gives $a_m(\Theta) = \exp \left\{ -j \frac{2\pi}{\lambda} (p_{x_m} \mu + p_{y_m} \nu + p_{z_m} \xi) \right\}$, where $\mu = \cos(\phi) \sin(\theta)$, $\nu = \sin(\phi) \sin(\theta)$, and $\xi = \cos(\theta)$. Evidently, $a_m(\Theta)$ is a multi-dimensional harmonic. Once the frequencies μ , ν , and ξ in different directions are estimated, the DoA angles are obtained using the relations

$$\theta = \tan^{-1} \left(\frac{\nu}{\mu} \right), \quad \phi = \cos^{-1} \left(\frac{\xi}{\sqrt{\mu^2 + \nu^2 + \xi^2}} \right), \quad (6.4)$$

with the usual ambiguity in $[0, 2\pi]$. In case of a linear array, there is only one parameter in the steering vector whereas two parameters are involved in planar and three-dimensional arrays.

In the context of sparse array selection, our goal is to choose the “best” K sensors in an M -element array in the sense that the lowest statistical mean-square-error (MSE), i.e., the CRB is achieved [69, 70]. Overall, $C = \binom{M}{K} = \frac{M!}{K!(M-K)!}$ possible subarray choices are available. Therefore, we can treat sensor selection as a classification problem with C classes. It seems impractical to visit all possible subarray configurations to arrive at the best subarray candidate. However, it has been shown [46, 18, 61] that many subarray candidates yield the same CRB level because of the non-unique placement of sensors within the array. Hence, the distinct number of subarrays is very small, which makes this technique very practical. Note that the literature suggests other statistical bounds [66] for DoA estimation but a closed-form solution of only CRB is available for higher dimensional arrays.

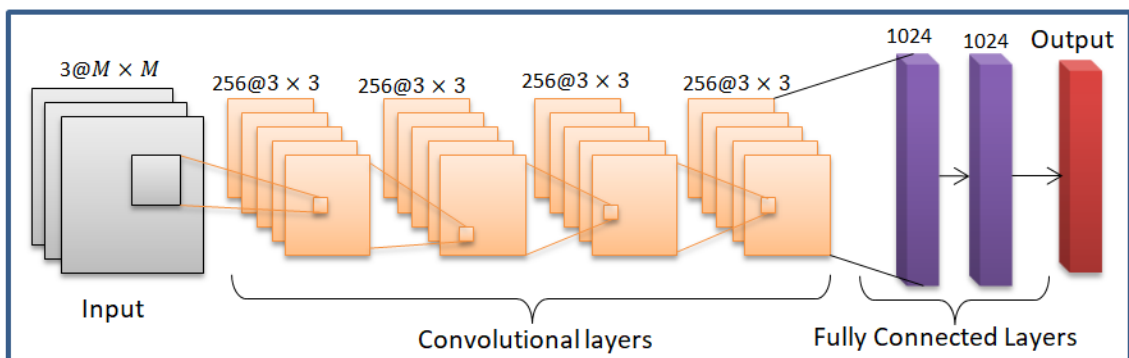


Figure 6.3: Structure of the CNN for sensor selection [72].

We observe Θ as the inner product $\mathbf{p}_m^T \mathbf{r}(\Theta)$. The exponential form of $a_m(\Theta)$ suggests that this is a multi-dimensional spatial harmonic whose frequencies (and hence, DoAs) can be extracted through conventional as well as sparse reconstruction algorithms [46, 9]. The uniqueness of spatial harmonic retrieval [71] is directly related to the number of sensors in the array. For a URA of size $M_1 \times M_2$, at least $M_1 M_2 - \min(M_1, M_2)$ sensors are required for a perfect DoA retrieval in a noiseless setting. Hence, in any sparse sensor array selection, K must satisfy these guarantees.

In general, the target's position changes little during consecutive scans while a phased array can switch very fast from one antenna configuration to the other. Here, we consider the following scan strategy for the radar: at the beginning (the very first scan), all M antennas are active and the received signal from this scan is fed to the network. Our goal is to find an optimal antenna array for the next scan in which only K antennas will be used. The radar continues to use this subarray for a few subsequent scans. After surveying the target scene with this optimal subarray for a predetermined number of scans, the radar switches back to the full array for a single scan. The received signal from this full array scan is then used to find a new, optimal subarray for the subsequent few scans. The frequency of choosing a new subarray can be decided off-line based on the nature of the target and analysis of previous observations. This switching of elements between different scans is a cognitive operation because a new array is determined in every few scans based on received echoes from the target scene.

6.3.2. Antenna Selection via Deep Learning

A DL network (see Fig. 6.3) is defined as a non-linear mapping which categorizes and clusters the input data. Let $\mathcal{D} = \{\mathcal{D}^{(1)}, \dots, \mathcal{D}^{(D)}\}$ and $\mathcal{Y} = \{\mathcal{Y}^{(1)}, \dots, \mathcal{Y}^{(Y)}\}$ denote the input and output labels for a dataset. Then, the deep classification network is represented as $\Sigma(\mathcal{D}) = \mathcal{Y}$ mapping the input data to the output labels which represent the best subarray indices.

Assume that an antenna subarray composed of K antennas is to be selected from an M -element antenna array. There are $C = \binom{M}{K}$ possible choices. This can be

viewed as a classification problem with C classes each of which represents a different subarray. Let $\mathcal{P}_k^c = \{p_{x_k}^c, p_{y_k}^c, p_{z_k}^c\}$, $k = 1, \dots, K$, be the set of the k th antenna coordinates in the c th subarray. Then, the c th class consisting of the positions of all elements in the c th subarray is

$$\mathcal{S}_c = \{\mathcal{P}_1^c, \dots, \mathcal{P}_K^c\}, \quad (6.5)$$

and all classes are given by the set

$$\mathcal{S} = \{\mathcal{S}_1, \mathcal{S}_2, \dots, \mathcal{S}_C\}. \quad (6.6)$$

Next, we design a CNN to solve this classification problem by selecting the positions of the antenna subarray that provides the best DoA estimation performance. Note that, for an operational radar, generation of an artificial or simulated dataset to train the DL network is not necessary. Instead, the network can train itself with the data acquired by the radar during previous scans. During the test phase, the DoA angles are unknown to the network. The CNN accepts the features from the estimated covariance matrix and outputs a new array. This stage is, therefore, cognitive because the radar is adapting the antenna array in response to the received signal. In the following, we present the details of input and output design of the deep network.

Input Data The input to the DL network are the covariance matrices of the received signal. In particular, we use the real, imaginary and the phase information of the covariance matrix. Let \mathbf{X} be an $M \times M \times 3$ real-valued matrix with 3 “channel”. Hence, we have $\mathcal{D}^{(i)} = \mathbf{X}$ for i -th input instant. Specifically, we define the (i, j) -th entry of the first and the second “channel” of the input data as $[\mathbf{X}_{(:, :, 1)}]_{i, j} = \text{Re}\{[\mathbf{R}]_{i, j}\}$ and $[\mathbf{X}_{(:, :, 2)}]_{i, j} = \text{Im}\{[\mathbf{R}]_{i, j}\}$, respectively, where \mathbf{R} is the array covariance matrix as

$$\mathbf{R} = \frac{1}{T} \sum_{i=1}^T \mathbf{y}(t_i) \mathbf{y}^H(t_i). \quad (6.7)$$

Similarly, the third “channel” is given by $[\mathbf{X}_{(:, :, 3)}]_{i, j} = \angle\{[\mathbf{R}]_{i, j}\}$. Although real and imaginary inputs are sufficient to describe the complex covariance matrix, feeding a third quantity such as phase (or magnitude) lets the network know that the first two inputs are related to each other.

Labeling We treat the sensor selection problem as a classification problem with C classes. The class label comprises the positions of the sensor subarray corresponding to that class. Let $\mathcal{P}_c^{(k)} = \{x_k^{(c)}, y_k^{(c)}, z_k^{(c)}\}$ be the set of sensor coordinates in the c -th subarray for $k = 1, \dots, K$. Then the positions of the sensors for the c -th class form the set $\mathcal{Y}_c = \{\mathcal{P}_c^{(1)}, \dots, \mathcal{P}_c^{(K)}\}$. Therefore, the set of all classes is $\mathcal{Y} = \{\mathcal{Y}_1, \mathcal{Y}_2, \dots, \mathcal{Y}_C\}$.

In order to select the best subarrays in \mathcal{Y} , we compute the CRB for each element of \mathcal{Y} as $c = 1, \dots, C$. Consider the $K \times 1$ subarray output

$$\mathbf{y}_c(t_i) = \mathbf{a}_c(\Theta) s(t_i) + \mathbf{n}_c(t_i), \quad (6.8)$$

Table 6.1: Number of classes C and the reduced number of classes \bar{C} for a UCA with $M = 16$.

	$K = 3$	$K = 4$	$K = 5$	$K = 6$	$K = 7$	$K = 8$
C	560	1820	4368	8008	11440	12870
\bar{C}	16	10	16	11	16	16

where $\mathbf{a}_c(\Theta) \in \mathbb{C}^K$ denotes the array steering vector corresponding to the subarray with position set \mathcal{Y}_c . Let $\mathbf{R}_c = \frac{1}{T} \sum_{i=1}^T \mathbf{y}_c(t_i) \mathbf{y}_c^H(t_i)$ be the $K \times K$ subarray sample covariance matrix for the $K \times 1$ subarray output $\mathbf{y}_c(t_i)$. We denote the partial derivatives of $\mathbf{a}_c(\Theta)$ with respect to θ and ϕ by $\dot{\mathbf{a}}_c(\theta) = \frac{\partial \mathbf{a}_c(\Theta)}{\partial \theta}$ and $\dot{\mathbf{a}}_c(\phi) = \frac{\partial \mathbf{a}_c(\Theta)}{\partial \phi}$, respectively. The signal and noise variances are σ_s^2 and σ_n^2 , respectively.

The CRBs for θ and ϕ in a single source scenario are [69]

$$\kappa(\theta, \mathcal{Y}_c) = \frac{\sigma_n^2}{2T \operatorname{Re} \left\{ \mathbf{\Pi}_\theta \odot (\sigma_s^4 \mathbf{a}_c^H(\Theta) \mathbf{R}_c^{-1} \mathbf{a}_c(\Theta)) \right\}}, \quad (6.9)$$

$$\kappa(\phi, \mathcal{Y}_c) = \frac{\sigma_n^2}{2T \operatorname{Re} \left\{ \mathbf{\Pi}_\phi \odot (\sigma_s^4 \mathbf{a}_c^H(\Theta) \mathbf{R}_c^{-1} \mathbf{a}_c(\Theta)) \right\}}, \quad (6.10)$$

where

$$\mathbf{\Pi}_\theta = \dot{\mathbf{a}}_c^H(\theta) \left[\mathbf{I}_K - \frac{\mathbf{a}_c(\Theta) \mathbf{a}_c^H(\Theta)}{K} \right] \dot{\mathbf{a}}_c(\phi), \quad (6.11)$$

$$\mathbf{\Pi}_\phi = \dot{\mathbf{a}}_c^H(\phi) \left[\mathbf{I}_K - \frac{\mathbf{a}_c(\Theta) \mathbf{a}_c^H(\Theta)}{K} \right] \dot{\mathbf{a}}_c(\theta). \quad (6.12)$$

We define the absolute CRB [73] for the directions Θ and \mathcal{Y}_c as the root-mean-square (RMS) value

$$\kappa(\Theta, \mathcal{Y}_c) = \frac{1}{\sqrt{2}} [\kappa(\theta, \mathcal{Y}_c)^2 + \kappa(\phi, \mathcal{Y}_c)^2]^{1/2}. \quad (6.13)$$

For simplicity, we select $\sigma_s^2 = 1$ and define the signal to noise ratio in the training data as $\text{SNR}_{\text{TRAIN}} = 10 \log_{10}(\sigma_s^2/\sigma_n^2)$.

Once $\kappa(\Theta, \mathcal{Y}_c)$ is computed for $c = 1, \dots, C$, the best subarray label $\mathcal{B}_{\bar{c}}$ is

$$\mathcal{B}_{\bar{c}} = \arg \min_{c=1, \dots, C} \kappa(\Theta, \mathcal{Y}_c). \quad (6.14)$$

Here, the subscript $(\cdot)_{\bar{c}}$ denotes the index of best subarrays, $\bar{c} = 1, \dots, \bar{C}$, where \bar{C} is the number of best subarrays. As K increases, C becomes very large. This makes the classification operation very difficult. However, experiments reveal that most of the sensor subarrays yield the same $\kappa(\Theta, \mathcal{Y}_c)$ because the non-unique sensor positions are common

Algorithm 1 Training data generation.

Input: Sensor positions $\{\mathbf{p}_m\}_{m=1}^M$, K , T , number of data realizations L , number of directions P and $\text{SNR}_{\text{TRAIN}}$.

Output: Training data \mathcal{T} with dimensions $\{M \times M \times 3 \times LP, LP\}$.

1: Generate P DoA angles $\Theta_p = (\theta_p, \phi_p)$ for $p = 1, \dots, P$.

2: **for** $1 \leq p \leq P$ **do**

3: **for** $1 \leq l \leq L$ **do**

4: Generate the array output $\{\mathbf{y}^{(l,p)}(t_i)\}_{i=1}^T$ as

$$\mathbf{y}^{(l,p)}(t_i) = \mathbf{a}(\Theta_p)s^{(l,p)}(t_i) + \mathbf{n}^{(l,p)}(t_i),$$

for $s^{(l,p)}(t_i) \sim \mathcal{CN}(0, \sigma_s^2)$, $\mathbf{n}^{(l,p)}(t_i) \sim \mathcal{CN}(0, \sigma_n^2 \mathbf{I})$.

5: Construct all $K \times 1$ subarray output configurations $\mathbf{y}_c^{(l,p)}(t_i)$ as in (6.8) from $\mathbf{y}^{(l,p)}(t_i)$ for $c = 1, \dots, C$.

6: Compute $\kappa(\Theta_p, \mathcal{Y}_c)$ for $c = 1, \dots, C$ by using the covariance matrices $\mathbf{R}_c^{(l,p)}$.

7: Using $\kappa(\Theta_p, \mathcal{Y}_c)$, find the best subarray index as $\mathcal{B}_{\bar{c}}^{(l,p)}$ from (6.14).

8: Compute the full array covariance matrix $\mathbf{R}^{(l,p)}$ from $\mathbf{y}^{(l,p)}(t_i)$, $i = 1, \dots, T$.

9: Construct the input data $\mathbf{X}^{(l,p)}$ as

$$[\mathbf{X}_{(:, :, 1)}^{(l,p)}]_{i,j} = \text{Re}\{[\mathbf{R}^{(l,p)}]_{i,j}\},$$

$$[\mathbf{X}_{(:, :, 2)}^{(l,p)}]_{i,j} = \text{Im}\{[\mathbf{R}^{(l,p)}]_{i,j}\},$$

$$[\mathbf{X}_{(:, :, 3)}^{(l,p)}]_{i,j} = \angle\{[\mathbf{R}^{(l,p)}]_{i,j}\}.$$

10: Design the output label as $z^{(l,p)} = \mathcal{B}_{\bar{c}}^{(l,p)}$.

11: **end for** l

12: **end for** p

13: Construct training data by concatenating the input-output pairs: $\mathcal{T} = \{(\mathbf{X}^{(1,1)}, z^{(1,1)}), (\mathbf{X}^{(1,2)}, z^{(1,2)}), \dots, (\mathbf{X}^{(1,L)}, z^{(1,L)}), (\mathbf{X}^{(2,1)}, z^{(2,1)}), \dots, (\mathbf{X}^{(P,L)}, z^{(P,L)})\}$.

in many subarray combinations. Hence, $\bar{C} \ll C$ implying that only a handful of classes yield the lowest estimation errors [46, 18]. In Table 6.1, we present the comparison of C and \bar{C} for a UCA with $M = 16$ antennas. We note that \bar{C} is very small, which leads to an effective classification performance. After computing all best subarray indices, we finally construct the best subarray set as $\mathcal{B} = \{\mathcal{B}_1, \dots, \mathcal{B}_{\bar{C}}\}$, where $\mathcal{B} \subset \mathcal{Y}$.

Algorithm 1 lists the steps to generate the training data by incorporating the input and labels, as discussed above. The training data is then fed to the deep network represented by $\Sigma(\cdot) : \mathbb{R}^{M \times M \times 3} \rightarrow \mathcal{Y}$ that maps the input data \mathbf{X} to the corresponding class in \mathcal{Y} .

Network Architecture Figure 6.3 illustrates the deep network architecture for sensor

selection. For a multi-layer network, the non-linear function $\Sigma(\cdot)$ is represented by the inner layers as

$$\Sigma(\mathcal{D}) = f^{(15)}(f^{(14)}(\dots f^{(2)}(f^{(1)}(\mathcal{D})))) = \mathcal{Y}, \quad (6.15)$$

where the first layer $f^{(1)}$ is the input layer and $f_{i \in \{2,4,6,8\}}^{(i)}$ denote the convolutional layers, each of which has 256 filters of size 3×3 . The arithmetic operation of a single filter of a convolutional layer is defined for an arbitrary input $\bar{\mathbf{X}} \in \mathbb{R}^{d_x \times d_x \times V_x}$ and output $\bar{\mathbf{Y}} \in \mathbb{R}^{d_y \times d_y \times V_y}$ as

$$\bar{\mathbf{Y}}_{p_y, v_y} = \sum_{p_k, p_x} \langle \bar{\mathbf{W}}_{v_y, p_k}, \bar{\mathbf{X}}_{p_x} \rangle, \quad (6.16)$$

where $d_x \times d_y$ is the size of the convolutional kernel, $V_x \times V_y$ is the size of the response of a convolutional layer, $\bar{\mathbf{W}}_{v_y, v_k} \in \mathbb{R}^{V_x}$ denotes the weights of the v_y -th convolutional kernel, and $\bar{\mathbf{X}}_{p_x} \in \mathbb{R}^{V_x}$ is the input feature map at spatial position p_x . Hence, we define p_x and p_k as the two-dimensional (2-D) spatial positions in the feature maps and convolutional kernels, respectively [74].

The 10-th and 12-th layer are fully connected with 1024 units whose 50% is randomly selected during training to avoid overfitting. A fully connected layer maps an arbitrary input $\bar{\mathbf{x}} \in \mathbb{R}^{U_x}$ to the output $\bar{\mathbf{y}} \in \mathbb{R}^{U_y}$ by using the weights $\bar{\mathbf{W}} \in \mathbb{R}^{U_x \times U_y}$. Then, the u_y -th element of the output of the layer is the inner product

$$\bar{y}_{u_y} = \langle \bar{\mathbf{W}}_{u_y}, \bar{\mathbf{x}} \rangle = \sum_i [\bar{\mathbf{W}}]_{u_y, i}^T \bar{x}_i, \quad (6.17)$$

for $u_y = 1, \dots, U_y$ and $\bar{\mathbf{W}}_{u_y}$ is the u_y -th column vector of $\bar{\mathbf{W}}$, and $U_x = U_y = 1024$ is selected for $f^{(14)}$.

After each convolutional and fully connected layers (i.e., $f_{i \in \{3,5,7,9,11,13\}}^{(i)}$), there is a rectified linear unit (ReLU) layer where $\text{ReLU}(x) = \max(0, x)$. The ReLU layers are powerful in constructing the non-linearity of the deep network as well as providing non-negative output at the output layers, which is very useful for classification networks. The 14-th layer has a classification layer with \bar{C} units, where a softmax function is used to obtain the probability distribution of the classes. The softmax layer is defined for an arbitrary input $\bar{\mathbf{x}} \in \mathbb{R}^D$ as $\text{softmax}(\bar{x}_i) = \frac{\exp\{\bar{x}_i\}}{\sum_{i=1}^D \exp\{\bar{x}_i\}}$. The last layer $f^{(15)}$ is the classification layer.

6.3.3. Numerical Experiments

We now investigate antenna selection performance of various array geometries such as UCAs and RDAs as shown in Fig. 6.4. The classification accuracies of training and validation data for UCA and RDA are listed in Table 6.2. We can see that the learning model achieves high accuracy when M is large and $\text{SNR}_{\text{TEST}} \geq 10\text{dB}$.

Figure 6.5 shows the classification performance of the CNN for $J_{\text{TEST}} = 100$ Monte Carlo trials. Figure 6.5 also shows the performance of the noisy test data when

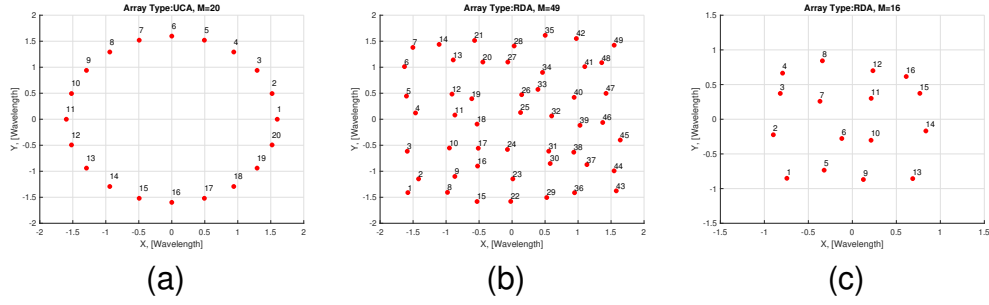


Figure 6.4: Placement of antennas for a) UCA with $M = 20$ elements, b) RDA with $M = 49$ and c) RDA with $M = 16$ [46].

the network is trained with noise-free dataset; its performance degrades especially at low SNR levels. These observations imply that noisy training datasets should be used for robust classification performance with the test data. On the other hand, when the training data is corrupted with strong noise content (e.g., $\text{SNR}_{\text{TRAIN}} \leq 10\text{dB}$), then despite using the noisy training data, the CNN model does not recover from poor performance at low SNR_{TEST} regimes. The performance at low SNRs can be improved when the size of the array increases and, as a result, the input data is huge and the SNR is enhanced due to large M . As an example, Fig. 6.5b illustrates the performance of the network for UCA with $M = 45$ and $K = 5$, where the network provides high accuracy for a wide range of SNR_{TEST} compared to the scenario in Fig. 6.5a.

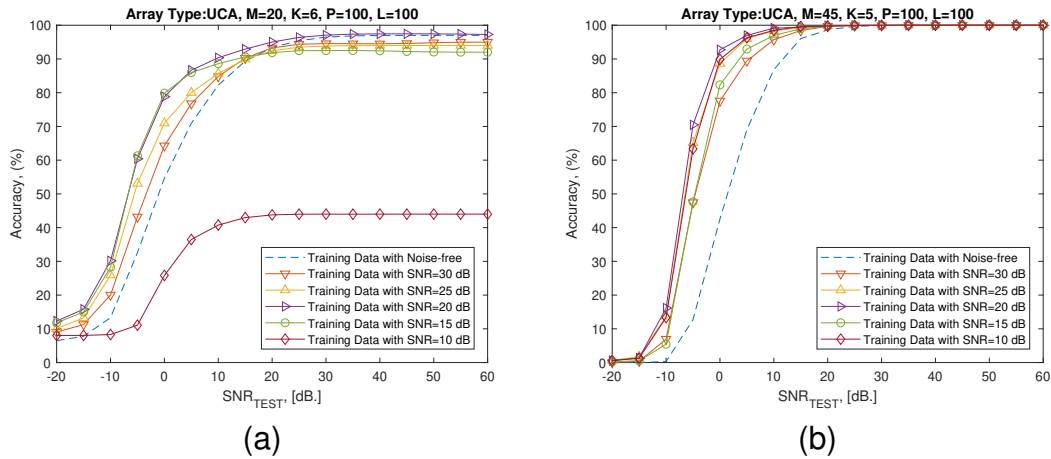


Figure 6.5: Performance of test dataset using CNN with respect to SNR_{TEST} for a UCA with (a) $M = 20$, $K = 6$, and (b) $M = 45$, $K = 5$, respectively [46].

DoA estimation performance of the DL-based scheme is also presented. The CNN approach is compared with support vector machine (SVM) and random antenna selection (RAS) algorithms. The selected antenna subarrays from CNN and SVM are inserted to the beamforming technique [75] for DoA estimation. As a traditional technique, we consider the RAS algorithm where, instead of all subarray candidates, a number of subarray

Table 6.2: The accuracy percentages for training and validation datasets in 1-D and 2-D scenario.

	1-D, UCA with $M = 20, K = 6$.		1-D, UCA with $M = 45, K = 5$.	
$\text{SNR}_{\text{TRAIN}}$	Training	Validation	Training	Validation
10 dB	65.2%	68.7%	98.7%	97.8%
15 dB	98.1%	98.5%	99.0%	98.7%
20 dB	99.2%	99.5%	100%	99.7%
25 dB	99.4%	99.8%	100%	100%
30 dB	100%	100%	100%	100%
inf dB	100%	100%	100%	100%
	1-D, RDA with $M = 49, K = 5$.		2-D, RDA with $M = 16, K = 6$.	
$\text{SNR}_{\text{TRAIN}}$	Training	Validation	Training	Validation
10 dB	97.8%	95.7%	8.1%	10.7%
15 dB	99.9%	98.6%	60.1%	63.2%
20 dB	97.5%	98.1%	80.8%	80.6%
25 dB	100%	100%	88.9%	89.2%
30 dB	100%	100%	82.6%	83.2%
inf dB	100%	100%	85.0%	83.9%

geometries are realized randomly (i.e., 1000 realizations) and their beamforming spectra is obtained by a search algorithm [76]. We also added the full array performance where $M = K$ for comparison. In Fig. 6.6a, the results are given for a UCA with $M = 20$ and $K = 6$ antennas to be selected. Here, "best subarray" denotes the beamforming performance of the subarray that gives the lowest CRB. It can be seen that CNN provides better performance as compared to SVM (32% more accurate) and RAS (72%) and it approaches the performance of the "best subarray" as expected from the accuracy results given in Fig. 6.5a. SVM performs poorer due to its lower antenna selection accuracy. We present 2-D DoA estimation results in Fig. 6.6b for RDA with $M = 16$ and $K = 6$. Similar observations are obtained for the 2-D case as compared to the 1-D scenario.

We further compare the DoA estimation performance of the selected subarrays with full array ($M = K$) performance in both Fig. 6.6a and Fig. 6.6b. While there is a gap between subarray and the full array performances, antenna selection provides less computation and cost.

We also analyze the effect of the performance metrics on the antenna selection and DoA estimation accuracy by employing the simplest and most common geometry of a ULA. For creating the training data, we employed three bounds: CRB, BZB and WWB [66]. The network was trained for $M = 10, K = 4, L_{\text{TRAIN}} = 100$ snapshots, $T_{\text{TRAIN}} = 100$ signal and noise realizations, and $P_{\text{TRAIN}} = 100$ DoA angles. The number of uniformly spaced azimuthal grid points are set to $P_{\phi} = 100$. For test mode, we fed the network with data corresponding to $P_{\text{TEST}} = 100$ DoA angles different than the

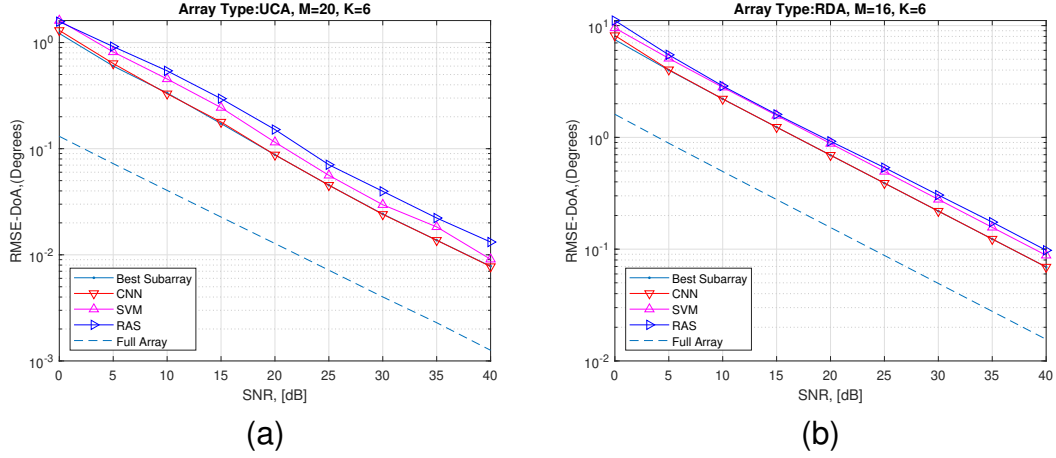


Figure 6.6: DoA estimation performance with respect to SNR. $\text{SNR}_{\text{TRAIN}} = 20$ dB. The antenna geometry is (a) UCA with $M = 20$ and $K = 6$, (b) RDA with $M = 16$ and $K = 6$ [46].

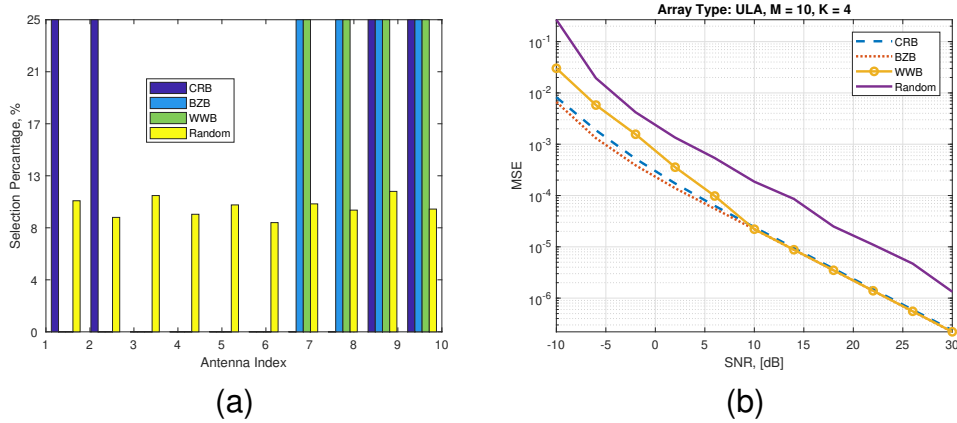


Figure 6.7: (a) Antenna selection percentage over $J_{\text{TEST}} = 10000$ trials. (b) MSE of DoA for selected subarrays. The array geometry is a ULA with $M = 10$ and $K = 4$ [46].

ones used in the training phase but keeping the values of M , K , L and T same as in the training. Fig. 6.7a shows the percentage of times a particular antenna index appears as part of the optimal array in the output over $J_{\text{TEST}} = T_{\text{TEST}}P_{\text{TEST}}$ trials with different performance metrics used during training. As seen here, when the CNN is trained with data created from the CRB, the classifier output arrays usually consists of the elements at the extremities. However, the network trained on BZB and WWB usually selects arrays with elements close to each other leading to low sidelobe levels. Also shown here is the random selection wherein each element is chosen with approximately 10% selection rate. We provide the DoA estimation performance of the antenna subarrays selected by the network for different values of test data SNRs in Fig. 6.7b. We observe that, compared to the DL-based approach, the random thinning results in inferior DoA estimation due to small array aperture. Among various bounds, the MSE is somewhat similar at high SNR

regimes with the BZB faring better than CRB at low SNRs.

6.4. TL for Sparse Arrays

The CNN architecture presented in the previous section is designed for a specific array geometry and is, therefore, inapplicable to different array configurations without significant re-training with new data. This arises from the assumption that the data used for training and testing are drawn from the same or similar distribution, which is difficult to guarantee in real world. In deep learning, this problem is called *domain mismatch* [77]. On the other hand, labeling sufficient training data for all possible application domains is prohibitive. It has been shown [78] that it is possible to establish a reasonable model by exploiting the labeled data drawn from another sufficiently labeled *source domain* which is closer to describing similar contents of the *target domain*. This *domain adaptation* (DA) enables knowledge transfer across domains. Lately, TL has emerged as an effective domain adaptation technique, wherein the DL network learns domain-invariant models across source and target domains [79], and has been applied to processing of image, bio-medical, radar, and speech signals.

Apart from a domain mismatch problem, networks such as a CNN also suffer from the need of a large training database. When only limited labeled data is available, the CNN fails to optimally select the sensor subarrays. Since CNN objective functions are highly non-convex and convergence of optimization algorithms to a global optimum is not guaranteed, training with only large data could increase the probability of convergence. Alternatively, training forms such as convolutional autoencoders (CAE) [80] and TL are employed in data-limited applications. Some studies [81] suggest that TL outperforms CAE especially when the sample sizes are very small.

In TL-based antenna selection, we address the domain mismatch between various array geometries and lack of massive training data by developing a more efficient, deep TL-based sensor subarray selection approach. Indeed, sufficient datasets required to support the level of training CNNs need are unavailable, expensive or impossible to extract in many real-world sensor array applications. We apply TL to enable the network in selecting sensor subarrays accurately even when limited labeled data are available. In particular, we transfer the features in the training data from one array geometry to a different array configuration. For example, we use a CNN trained with a URA to select sensors in a UCA. This domain transfer is advantageous when a large off-line database is required for system identification or calibration [82].

Conventionally, DoA estimation across various geometries is performed with array transformation and array interpolation techniques [83]. However, for multiple targets and complex geometries, these techniques are difficult to come by [84, 85]. TL-based approach is helpful in overcoming such limitations.

When compared with the domain transfer in shallow TL techniques [86], such as classification based on SVM, a deep TL approach combines DA with the power of a deep network to learn the explanatory factors of variations in data and reduce the mismatch between the marginal distributions across array geometries. In Fig. 6.8, we define the

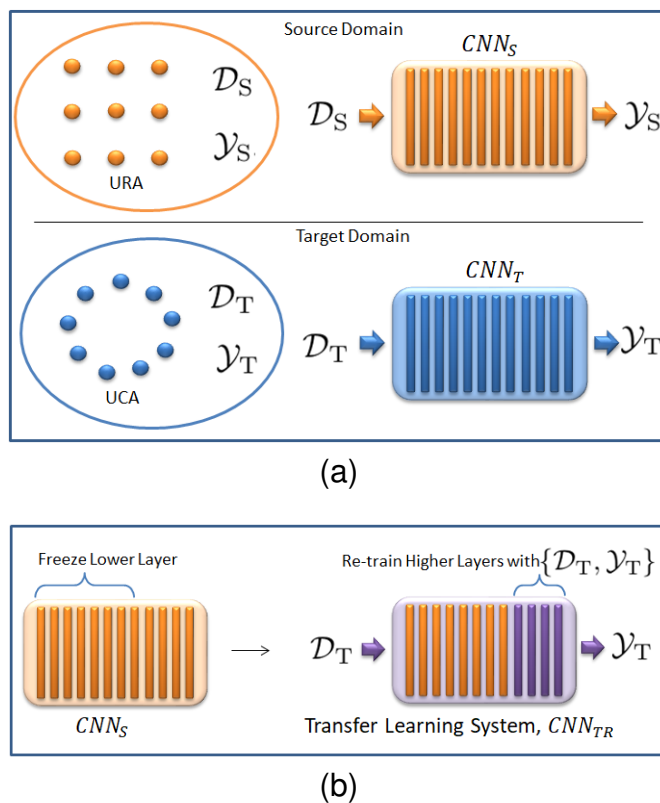


Figure 6.8: The representation of the source and target domains for knowledge transfer from, for example, URA to UCA configuration. (a) Source (top) and target (bottom) domain data with corresponding learning networks CNN_S and CNN_T , respectively. (b) In deep TL, lower layers of CNN_S are frozen and only higher layers are re-trained with the target domain (UCA) data $\{\mathcal{D}_T, \mathcal{Y}_T\}$ to transfer sensor selection knowledge from source domain (URA) [72].

source (target) data and labels as \mathcal{D}_S (\mathcal{D}_T) and \mathcal{Y}_S (\mathcal{Y}_T), respectively. We train the source network CNN_S , which learns the non-linear relationship between \mathcal{D}_S and \mathcal{Y}_S as

$$\mathcal{Y}_S = \Sigma_S(\mathcal{D}_S), \quad (6.18)$$

where $\Sigma_S(\cdot)$ is the non-linear function that constructs the mapping between the data and labels in the source domain. In (6.18), the label data are the positions of the best subarray sensors as $\mathcal{Y}_S = \{\mathcal{Y}_S^{(1)}, \mathcal{Y}_S^{(2)}, \dots, \mathcal{Y}_S^{(S)}\}$ where $S = |\mathcal{Y}_S| = |\mathcal{D}_S|$ is the number of elements in the source domain. Furthermore, \mathcal{D}_S is the collection of covariance matrices of the array outputs of the source array geometry, i.e.,

$$\mathcal{D}_S = \{\mathcal{D}_S^{(1)}, \mathcal{D}_S^{(2)}, \dots, \mathcal{D}_S^{(S)}\}, \quad (6.19)$$

where $\mathcal{D}_S^{(i)} = \mathbf{X}_S$ which is constructed from the source domain covariance matrix

$$\mathbf{R}_S = \frac{1}{T} \sum_{i=1}^T \mathbf{y}_S(t_i) \mathbf{y}_S^H(t_i), \quad (6.20)$$

Algorithm 2 Transfer learning for sensor selection.

Input: $\{\mathcal{D}_S, \mathcal{Y}_S\}, \{\mathcal{D}_T, \mathcal{Y}_T\}$

Output: CNN_{TR} .

- 1: Train CNN_S with $\{\mathcal{D}_S, \mathcal{Y}_S\}$.
 - 2: Construct TL network CNN_{TR} whose convolutional layers are designated the same as of CNN_S , i.e., $f_{\text{TR}_{i \in \{2,4,6,8\}}}^{(i)} = f_{S_{i \in \{2,4,6,8\}}}^{(i)}$.
 - 3: Train the remaining layers of the TL network with $\{\mathcal{D}_T, \mathcal{Y}_T\}$. Then, use CNN_{TR} for sensor selection for target domain data.
-

where $\mathbf{y}_S(t_i)$ denotes the array output of the source data.

Similarly, the target domain data and labels are $\mathcal{D}_T = \{\mathcal{D}_T^{(1)}, \mathcal{D}_T^{(2)}, \dots, \mathcal{D}_T^{(T)}\}$ and $\mathcal{Y}_T = \{\mathcal{Y}_T^{(1)}, \mathcal{Y}_T^{(2)}, \dots, \mathcal{Y}_T^{(T)}\}$, respectively, where $T = |\mathcal{D}_T|$ and $\mathbf{R}_T = \frac{1}{T} \sum_{i=1}^T \mathbf{y}_T(t_i) \mathbf{y}_T^H(t_i)$. For the target network CNN_T , we have

$$\mathcal{Y}_T = \Sigma_T(\mathcal{D}_T). \quad (6.21)$$

The TL framework assumes that the source domain has much larger dataset than the target domain, i.e., $S \gg T$. This implies that CNN_S will turn out to be a well-trained deep network whereas CNN_T has poor mapping performance and does not reflect the same mapping profile as CNN_S . To improve the performance of CNN_T , the key idea is to use the sensor selection ability of the pre-trained network CNN_S even if it is trained with different array data [87]. This is achieved by re-training CNN_S with the target domain data $\{\mathcal{D}_T, \mathcal{Y}_T\}$ while freezing the lower layers (i.e., convolutional layers) of CNN_S^2 . The new deep transfer network is CNN_{TR} (Fig. 6.8b). The lower layers are kept intact or *frozen* because they are generally domain invariant³ and hence, harbor the bulk of sensor selection knowledge. The higher layers, however, are largely domain variant such that when new labels are added to the problem (i.e., \mathcal{Y}_S is replaced with \mathcal{Y}_T), they require re-training. This approach accelerates the computation of the gradient in the backpropagation stage. Furthermore, it allows us to enlarge the feature space of the deep network without causing large error on the already-learned features [87].

Knowledge Transfer Across Different Array Geometries Once CNN_S (i.e., $\Sigma_S(\cdot)$) is trained with the source domain data, we freeze the weights in the $\{2, 4, 6, 8\}$ -th layers (i.e., the convolutional layers) to preserve the sensor selection ability of the deep network before transferring it to the target domain. We construct the TL network such that

$$\Sigma_{\text{TR}}(\mathcal{D}_T) = f^{(15)}(f^{(14)}(\dots \tilde{f}^{(2)}(f^{(1)}(\mathcal{D}_T)))) = \mathcal{Y}_T, \quad (6.22)$$

where the frozen layers are $\tilde{f}_{i \in \{2,4,6,8\}}^{(i)}$. Algorithm 2 lists these steps of the TL approach.

²We do not freeze the layers $\{3, 5, 7\}$, because they are ReLU layers with no weight to freeze.

³“Domain invariance” implies that when new labels are added to the network, the lower layers remain unaffected even though the problem has changed.

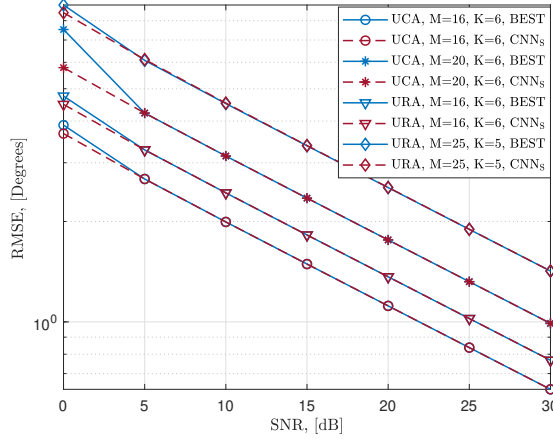


Figure 6.9: DoA estimation performance for CNN_S for different array geometries [72].

Deep Network Realization and Training For training, we used stochastic gradient descent algorithm with momentum 0.9 and updated the network parameters at learning rate 0.01 and mini-batch size of 512. The loss function was the cross-entropy cost

$$C_E = -\frac{1}{\bar{T}} \sum_{t=1}^{\bar{T}} \sum_{c=1}^{\bar{C}} \left[\chi_c^{(t)} \ln \eta_c^{(t)} + (1 - \chi_c^{(t)}) \ln(1 - \eta_c^{(t)}) \right], \quad (6.23)$$

where \bar{T} is the length of the dataset and $\{\eta_c^{(t)}, \chi_c^{(t)}\}_{t=1, c=1}^{\bar{T}, \bar{C}}$ is the input-output pair for the classification layer. It is worth noting that the cost function in (6.23) can be defined in terms of RMSE of DoA estimation procedure. However, this makes the training process problem-dependent. During training, the training data is shuffled for each epoch until training is terminated. Further, 80% and 20% of all generated data are chosen for training and validation datasets, respectively. The training rate is reduced by a factor of 0.9 after each 10 epochs. The training stops when the validation accuracy does not improve for three consecutive epochs.

To train CNN_S , we collected array data for $P_S = 100$ equally spaced direction in the sector $\tilde{\Theta} = [0^\circ, 359^\circ]$ azimuth plane and $L_S = 100$ noisy data realizations with $T = 100$ data snapshots. During training, we set $\sigma_s^2 = 1$ and use different SNR levels, namely, $\text{SNR}_{\text{TRAIN}} \in \{15, 20, 25\}$ dB. Hence, the total training data length is $3L_S P_S = 30000$. Once CNN_S is trained, the CNN_{TR} is constructed by following the steps in Algorithm 2. For the above-mentioned settings with $M = 16$ and $K = 6$, the training time for CNN_S , CNN_T are approximately 40 and 5 minutes respectively, whereas the TL network CNN_{TR} needs only 5 seconds to be trained.

6.4.1. Performance in Source Domain

We first present the performance of the CNN approach for the source domain case where different array geometries such as URA and UCA are considered with different array

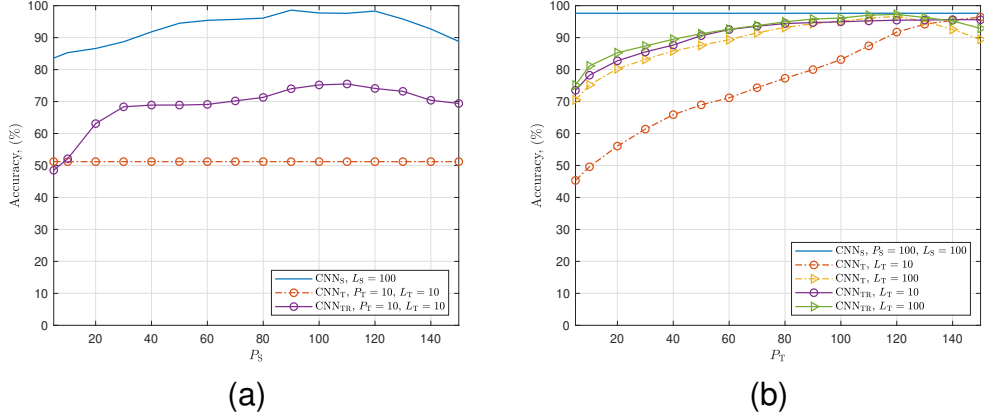


Figure 6.10: Performance of CNN_S , CNN_T and CNN_{TR} versus the number of DoA angles. Sensor selection accuracy is given with respect to (a) P_S when $L_S = 100$, $L_T = 10$, and (b) P_T when $P_S = 100$, $L_S = 100$. $\text{SNR}_{\text{TRAIN}} = 15$ dB [72].

settings. In particular, we consider sensor arrays with half wavelength sensor spacing for both UCA and URA. When CNN_S are trained for different arrays, we obtained above 90% validation accuracy for the training data in all cases. In the prediction stage, the DoA angles are generated uniformly at random in the interval $\tilde{\Theta}$ so that the DoA angles in the training and prediction are selected from the same distribution. After feeding CNN_S with these input data, the selected subarrays are obtained from the output for each scenario. Then, the sensor outputs of corresponding subarrays are employed for DoA estimation using MUSIC (MULTiple SIGNAL Classification) algorithm [88]. During the simulations in the prediction state, the network is tested for different SNR levels for $J_T = 100$ Monte Carlo trials. Figure 6.9 shows the RMSE in DoA estimation, i.e.,

$$\text{RMSE} = \left(\frac{1}{J_T} \sum_{j=1}^{J_T} (\hat{\phi}^{(j)} - \phi)^2 \right)^{\frac{1}{2}}, \quad (6.24)$$

where $\hat{\phi}^{(j)}$ and ϕ denote the estimated and true DoA angles, respectively. We compare the DoA estimation performance of CNN_S with the best subarray that provides the lowest CRB. Figure 6.9 demonstrates that CNN_S asymptotically follows the best subarray performance.

6.4.2. Performance for Transfer Learning

In order to evaluate the TL performance, we trained CNN_S with different sizes of datasets and then constructed CNN_{TR} from CNN_S for sensor selection. We considered URA and UCA geometries with $M = 16$, $K = 6$ for source and target domains, respectively.

Table 6.3: Training Validation Accuracy (%) For Different TL Scenarios

TL Scenario (Source \rightarrow Target)	Validation Accuracy (%)	
	CNN _T	CNN _{TR}
UCA \rightarrow URA, $M = 16, K = 6$	54.9	70.1
URA \rightarrow UCA, $M = 16, K = 6$	42.3	79.8
UCA \rightarrow $\overline{\text{UCA}}$, $M = 20, K = 6$	63.1	98.8
URA \rightarrow $\overline{\text{URA}}$, $M = 25, K = 5$	55.2	77.4

Fig. 6.10 shows the sensor selection accuracy

$$\text{Accuracy}(\%) = \frac{\text{U}}{\text{V}} \times 100, \quad (6.25)$$

where V is the total number of input datasets in which the model identified the best sub-arrays correctly U times. In Fig. 6.10a, the target domain \mathcal{D}_T are generated for $P_T = 10$ grid points in $\tilde{\Theta}$ and $L_T = 10$ and we varied P_S from 5 to 150 for \mathcal{D}_S with $L_S = 100$. For all three networks, The performance of CNN_T is fixed because \mathcal{D}_T does not change during the simulations. When P_S is very small (i.e., < 10), CNN_{TR} performs even worse than CNN_T. However, as P_S increases, CNN_{TR} and CNN_S exhibit higher selection accuracy. For large source datasets, e.g. $P_S \in [80, 120]$, CNN_{TR} outperforms CNN_T by a large margin because of the learned and transferred features from CNN_S. The increase in P_S does not necessarily improve the sensor selection performance because when the training data are densely sampled (i.e., P_S is high) the deep network cannot distinguish the input data of different directions and produce inaccurate classification output. These results suggest that CNN_S needs to be trained with at least $\mathbf{S} = P_S L_S = 40 \cdot 100 = 4000$ to provide satisfactory accuracy (e.g., above 90%). As a result, $P_S = 100$ is a reasonable choice for TL, wherein the target dataset 1000 times smaller, i.e., $\frac{\mathbf{S}}{\mathbf{T}} = \frac{L_S P_S}{L_T P_T} = 1000$. In Fig. 6.10b, we repeat the same analysis for CNN_T where we assume that CNN_S is well-trained with $P_S = 100$ and $L_S = 100$. Then, we sweep P_T similarly for both $L_T = 10$ and $L_T = 100$. We can see that when $L_T = 100$, CNN_T quickly reaches maximum similar to CNN_S as illustrated in Fig. 6.10a. In this case, the improvement gained by TL is incremental because CNN_T is already well-trained. However, if small dataset is used, i.e., $L_T = 10$, then it requires larger P_T to reach high accuracy. Expectedly, this analysis shows that TL provides reasonable improvement if the target dataset is relatively small, i.e., $\mathbf{T} = P_T L_T \leq 1000$ ($\mathbf{S} = 10000$). In other words, when \mathbf{T} is high there is no need to use TL. Therefore, in the following experiments, we select $P_T = L_T = 10$ and employ TL to improve the performance.

Table 6.3 lists the validation accuracy of CNN_T and CNN_{TR} for different TL scenarios. We consider TL between UCA and URA as well as the perturbed array geometries denoted by $\overline{\text{UCA}}$ and $\overline{\text{URA}}$. In a perturbed array geometry, the m -th sensor position is selected uniformly at random as $\{\tilde{x}_m, \tilde{y}_m, \tilde{z}_m\} \sim \mathcal{N}(\{x_m, y_m, z_m\}, (\lambda/4)^2)$ for each instance of the training data. It is evident that the sensor selection accuracy of CNN_{TR} is approximately 20% higher than CNN_T.

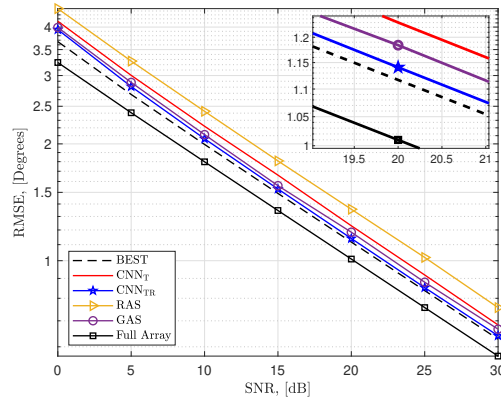


Figure 6.11: DoA estimation performance when source domain has URA; target domain has UCA geometry when $M = 16$, $K = 6$ [72].

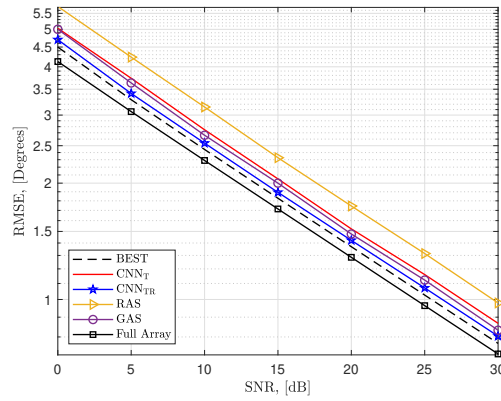


Figure 6.12: DoA estimation performance when source domain has UCA; target domain has URA geometry when $M = 16$, $K = 6$ [72].

We further assessed the DoA estimation performance of the selected subarrays for target domain data. For $M = 16$, $K = 6$, Figs. 6.11 and 6.12 depict the performance for URA \rightarrow UCA and UCA \rightarrow URA scenarios, respectively. We compared the sensor selection performance of CNN_T and CNN_{TR} with greedy-based antenna selection (GAS) [44], random selection (RAS) as well as the fully array performance. As expected, we see that the full array has the lowest SNR due to large array aperture. We observe that CNN_{TR} closely follows the performance of the best subarray. The CNN_{TR} exhibits approximately 4%, 8.5% and 23% lower RMSE as compared to GAS, CNN_T and RAS, respectively. It is worth noting that RAS has no rule on selecting the antennas while GAS is a greedy-based suboptimum method seeking the best subarray based on the CRB information [44]. These results establish the effectiveness of TL for DoA estimation with sensor selection. The superior performance of CNN_{TR} is because of the learned and transferred features from source domain data via CNN_S .

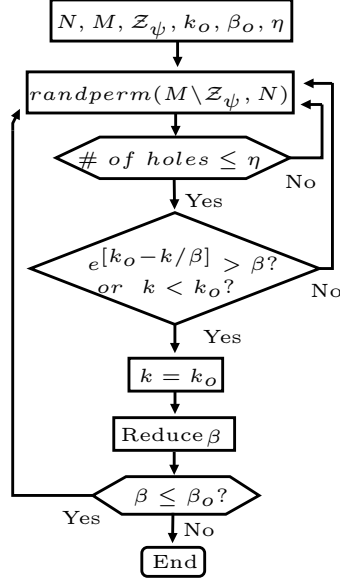


Figure 6.13: Improved SA algorithm for random 2D sparse subarray generation and optimization.

6.5. Large Planar Sparse Array Design with SA-Assisted DL

The SA-assisted DL-based approach was originally presented in [89, 90] to optimize sensor positions while minimizing the mutual coupling between the sensors. It was extended to 2-D sparse array design in [91]. Here, given an initial array as \mathcal{Z}_{init} , the optimized array \mathcal{Z}_{SA} is obtained by minimizing

$$\mathcal{Z}_{SA} = \underset{\mathcal{Z}_{init}}{\operatorname{argmin}} k_o = \sum_{i=1}^M \sum_{j=i+1}^M \frac{1}{\|m_i - m_j\|_2}, \quad (6.26)$$

$$\text{such that } \|m_i - m_j\|_2 \leq B,$$

where $m_i, m_j \in \mathcal{Z}_{init}$, M is the number of sensors, $\|\cdot\|_2$ is the l_2 -norm of a vector and B is the mutual coupling coefficient upper-bound. The SA algorithm is used as an initialization step for the deep learning model, mainly to generate sparse subarrays with large physical apertures and well-distributed sensors instead of an enumeration approach.

Figure 6.13 summarizes the step-by-step procedure of the flow diagram. Note that this SA-based approach can be extended to any planar array configuration, and the same applies to the whole SA-based initialization method [91]–[90]. The best subarrays are selected from \mathcal{H}_{sa} with the lowest CRB values as labels.

The whole algorithm is summarized in the Algorithm 3. The inputs are as follows: the total number of given antennas M , the number of antennas to be selected K , the number of snapshots T , the number of different DOA angles D , the number of signals and noise realizations P and the SNR. Moreover, the elements of \mathcal{V} are chosen from \mathcal{H}_{sa}

Algorithm 3 Training Dataset Generation Method

Input: N, M, T, K, P and $\text{SNR}_{\text{TRAIN}}$

Output: Training data $\mathcal{D}_{\text{TRAIN}}$

- 1: Generate \mathcal{H}_{sa} as shown in Fig. 6.13.
 - 2: Sample D DOA angles $\{\Theta_d\}_{d=1}^D$.
 - 3: Compute P different realizations of subarray output, $\{\mathbf{X}_d^i\}_{i=1}^P$ for $d = 1, \dots, D$
 - 4: $\mathbf{X}_d^i = [\mathbf{x}_d^i(1), \mathbf{x}_d^i(2), \dots, \mathbf{x}_d^i(T)]$,
 - 5: where $\mathbf{x}_d^i(t) = \mathbf{a}(d)\mathbf{s}^{(i)}(t) + \mathbf{n}^{(i)}(t)$,
 - 6: $\mathbf{s}^{(i)}(t) \sim \mathcal{CN}(0, \sigma_s^2 \mathbf{I})$ and $\mathbf{n}^{(i)}(t) \sim \mathcal{CN}(0, \sigma_n^2)$
 - 7: Calculate sample covariance matrix $\hat{\mathbf{R}}$ and $N \times N$ covariance matrices $R_{h_s}^{(i,d)}$ for $h_s = 1, 2, \dots, \mathcal{H}_{sa}$.
 - 8: Compute $\mathcal{C}(\Theta, \mathcal{Z}_{h_s})$ for all $h_s \in \mathcal{H}_{sa}$ and select subarrays.
 - 9: Create input-output data pairs as $(\hat{\mathbf{R}}^{(i,d)}, u_d^{(i)})$ for $d = 1, 2, \dots, D$ and for $i = 1, 2, \dots, P$.
 - 10: Connect the input-output pairs to form the training dataset as
 - 11: $\mathcal{D}_{\text{TRAIN}} = [(\hat{\mathbf{R}}^{(1,1)}, u_1^{(1)}), (\hat{\mathbf{R}}^{(2,1)}, u_1^{(2)}), \dots$
 - 12: $, (\hat{\mathbf{R}}^{(P,1)}, u_1^{(P)}), (\hat{\mathbf{R}}^{(1,2)}, u_2^{(1)}), \dots, (R^{(P,D)}, u_D^P)]$
 - 13: where the size of the training dataset is $\mathcal{R} = PD$.
-

which is calculated using the SA-based optimization method as shown in Fig. 6.13 rather than the enumeration of the entire combinations like in \mathcal{H} . The SNR used for calculation of the covariance matrices is denoted as $\text{SNR}_{\text{TRAIN}}$.

The performance of the SA-assisted DL-based antenna selection approach is evaluated through simulation. The problem of selecting $K = 16$ sensors out of a $N = 42 = 6 \times 7$ sensor URA is considered. The details of training and testing specifications can be found in [91].

The estimation accuracy of the SA-assisted DL-based method is evaluated in comparison to the conventional approach using the CNN models trained. Figure 6.14 shows the array configuration of predicted 2-D sparse arrays. Particularly, Fig. 6.14 (a) illustrates the parent 42–element URA whereas Fig. 6.14 (b)–(d) show the realized 16–element DL-based 2D sparse array using the conventional and DL-based method respectively.

Here, the performance of the realized 2-D sparse arrays is evaluated. In particular, we explore the behavior of the RMSE as a function of SNR and the number of snapshots. The RMSE is defined as

$$\text{RMSE} = \sqrt{\frac{1}{\mathcal{T}D} \sum_{i=1}^{\mathcal{T}} \sum_{d=1}^D [(\tilde{\phi}_d^i - \phi_d) + (\tilde{\theta}_d^i - \theta_d)]^2}, \quad (6.27)$$

where $\tilde{\phi}_d^i, \tilde{\theta}_d^i$ and ϕ_d, θ_d denote the estimated and true d –th DOAs in the i –th trial, respectively.

Table 6.4 lists the parameters used to compute RMSE with respect to SNR (Ex-

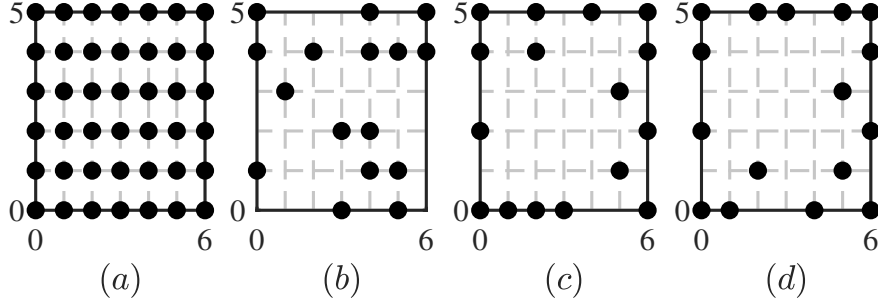


Figure 6.14: The array configurations of (a) parent 42–sensor URA, (b) the conventional DL-based array (16–sensors), (c) the conventional SA-based array (16–sensors) and (d) the DL-based array (16–sensors). Note that the dots denote physical sensors.

ample #1) and the number of snapshots (Example #2), respectively. Moreover, the 2-D-ESPRIT algorithm is used to estimate the sources. However, if the DCA of the realized 2-D arrays has holes in the coarray, the resulting virtual 2-D array becomes irregular. Therefore, the spatial-smoothing DOA estimation method such as 2-D-ESPRIT cannot be applied. This is the case as the 2-D-ESPRIT algorithm requires a URA array structure for spatial smoothing pre-processes. As a result, a nuclear norm minimization (NNM) approach [92] is applied to fill the holes to restore a standard 2-D configuration.

Figure 6.15 shows the DOA estimation performance of the realized DL-based 2D sparse array compared to the parent URA and other 2D sparse arrays. It can be observed in Fig. 6.15 (a) that the URA with 42 sensors has better performance overall due to the large physical aperture. In contrast, the performance of the DL-based 2D sparse array realized using the DL-based method has better than a URA with 16 sensors and slightly lower than that of the parent URA. Besides, the 2D sparse array performs better than the conventional SA-based sparse array. Moreover, the conventional DL-based performed poorly as compared to both the DL-based array and 16–sensor URA.

Table 6.4: 2-D DOA Estimation Simulation Parameters

Parameters	Simulation Examples	
	Example #1	Example #2
# of sources D	9	
# of trials, \mathcal{T}	1000	
# of snapshots	500	10 to 1000
SNR [dB]	–20 to 10	0
DOAs (θ, ϕ) [deg.]	(10, 255), (45, 300), (20, 345), (50, 210), (70, 0), (0, 30), (60, 165), (5, 120), (30, 79)	
Estimator	2-D-ESPRIT	

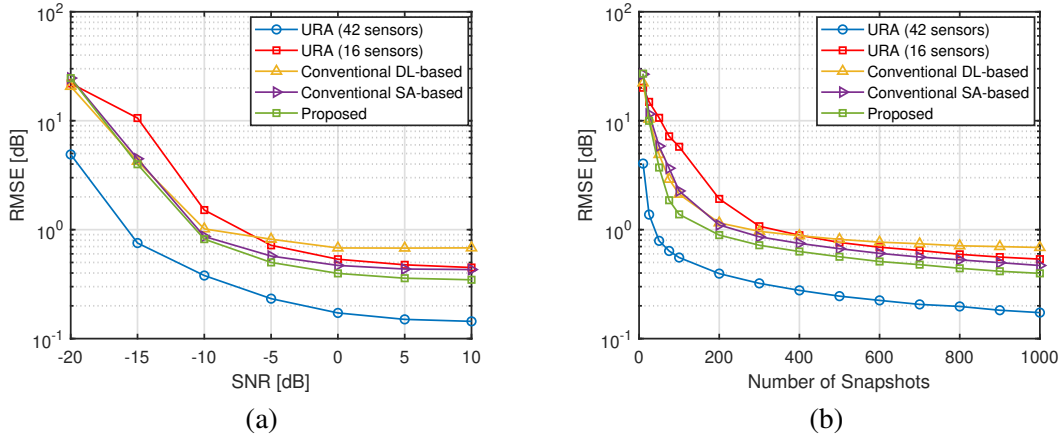


Figure 6.15: RMSE performance versus (a) SNR and (b) number of snapshots for the realized DL-based sparse array compared to URA, conventional DL-based array and SA-based array.

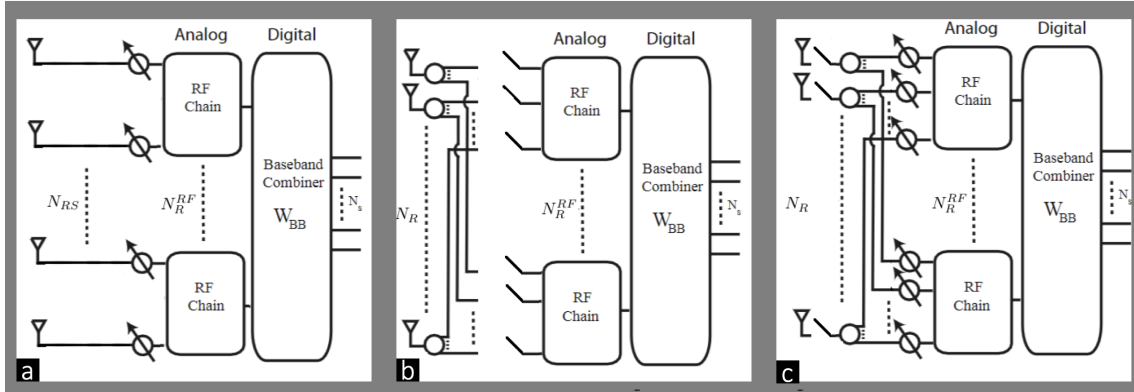


Figure 6.16: Receiver architectures with antenna selection for single user mmWave MIMO systems. (a) Scheme 1: Fixed subarray with fully-connected phase shifters. (b) Scheme 2: Switching network without optimized antenna selection and no phase shifters. (c) Scheme 3: Switching network with optimized antenna selection and phase shifters [18].

In Fig. 6.15 (b), we can observe a similar trend where the performance of the DL-based array is bounded by the parent URA and the 16–sensor URA as the number of snapshots increases. The parent URA has the lowest RMSE values, whereas the 16–sensor URA has higher RMSE values than the DL-based array. Also, the conventional DL-based array performs better than the 16–sensor URA in lower numbers of snapshots. However, the RMSE values degrade as the number of snapshots increases. These examples demonstrate that the DL method can thin 2-D arrays cognitively to a manageable size without considerable loss of DOA estimation resolution.

6.6. DL-based Sparse Array Design for Hybrid Beamforming

DL may also be used to simultaneously select antenna elements and design hybrid beamformers for massive MIMO wireless communications [18]. Here, we employ a CNN for each task. As before, the element selection problem is cast as a classification [93]. We then include the hybrid beamformer design in this DL framework by exploiting the structure

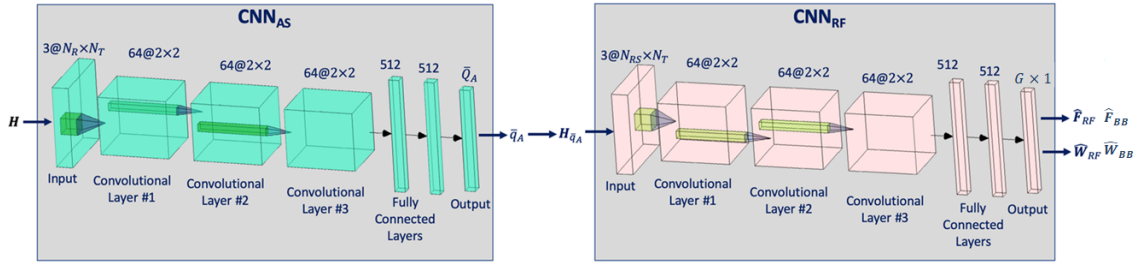


Figure 6.17: The CNN architecture for antenna selection and RF beamformer design [18].

of analog beamformers which are obtained by minimizing the cost between hybrid and unconstrained beamformers. The optimization problem is cast jointly with the antenna selection problem and it is solved by MATLAB-based Manopt algorithm [94] via manifold optimization (MO) [95].

Among the prevalent architectures for sparse array beamformers, a popular scheme is to employ a predetermined subarray with N_{RS} antennas selected from a full array of N_R elements (Fig. 6.16a). Each subarray feeds into a fully-connected phase shifter network of size N_R^{RF} with a single RF chain. This has the complexity of phase shifters but the antenna selection process is not optimized. Another common receiver architecture feeds the antennas directly to the RF chains thereby eliminating the phase shifters completely. Here, each RF chain is connected to the N_R antennas of which N_{RS} elements are selected using switches (Fig. 6.16b). In this case, the entries of the combiner matrix are either 1 or 0 to indicate the selected or unselected antennas, respectively. This is the simplest structure with no phase shifters. However, the antenna selection is not optimized and the elements are determined by simply choosing the largest absolute values in each column of the channel matrix. Finally, Fig. 6.16c shows a receiver that employs a switching network with phase shifters. In this system, a subarray with N_{RS} antennas is selected from a full array comprising N_R antennas. The subarray is connected to a phase shifter network of size N_R^{RF} which may apply an optimization procedure for antenna selection to achieve greater efficiency.

In this formulation, a CNN accepts channel matrix as input and provides the subarray that maximizes the spectral efficiency. Once the antenna selection (CNN_{AS}) is finalized (see Fig. 6.17), the corresponding partial channel matrix is fed to a second CNN (CNN_{RF}) which then chooses the best RF beamformer and constructs the corresponding baseband beamformer. To train both CNN models, different realizations of the channel matrix are used and the input data are labeled by the selected subarray/RF chains with the highest spectral efficiency. Even though DL network structures require channel matrix as an input, precise knowledge of this matrix is only required in the training stage to obtain the labels of the network. In the prediction stage, where the RF beamformers are estimated, precise channel knowledge is not necessary. Both CNNs are trained with channel matrices generated for different user location, channel gains and number of user clusters. Furthermore, each realization of channel matrix in the training data is corrupted by synthetic noise so that the performance of the learning network does not deteriorate with noisy test inputs.

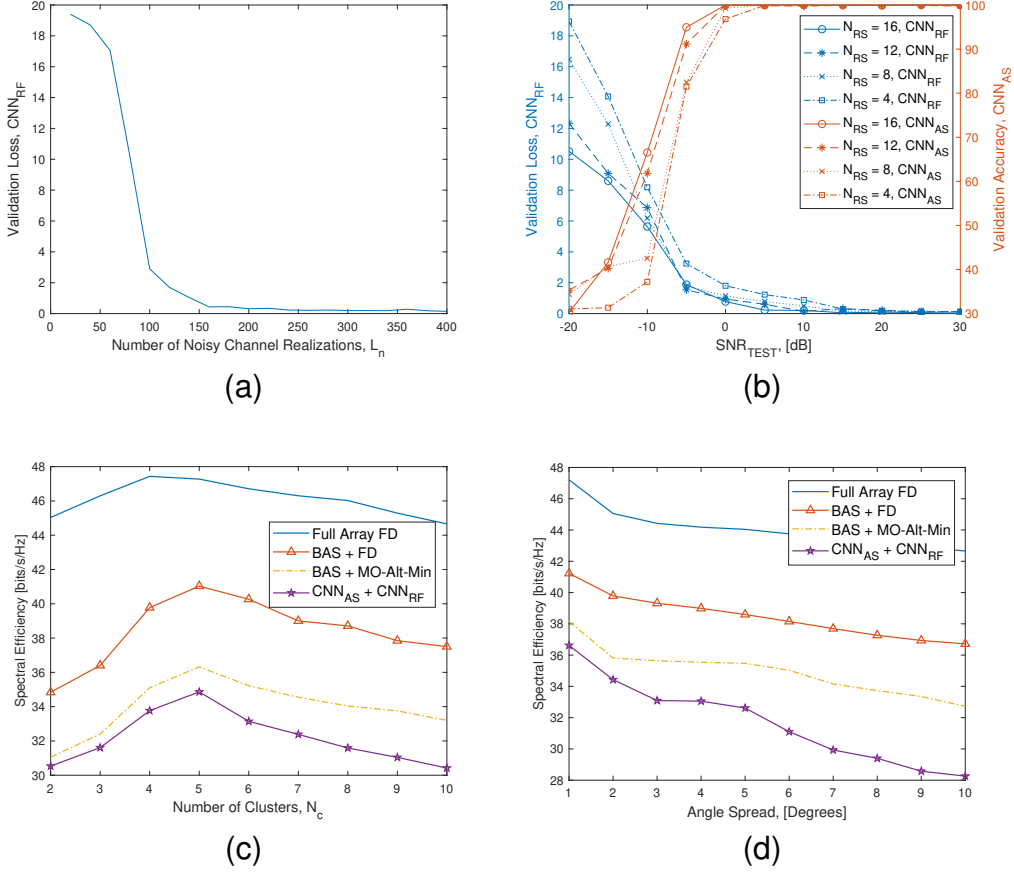


Figure 6.18: Performance of CNN. (a) Validation loss versus number of channel realizations L_n . (b) Validation loss for CNN_{RF} and validation accuracy for CNN_{AS}. (c) Spectral efficiency versus number of clusters in when the angle spread is $\sigma_\Theta^2 = 5^\circ$. (d) Spectral efficiency versus angle spread when the number of paths $N_c = 4$. We set the number of antennas as $N_T = N_R = 64$ with $N_{RS} = 16$ selected antennas [18].

Figure 6.18 summarizes the assessment of the performance of unquantized CNN. Here, we set $N = 100$, $N_T = N_R = 64$ and $N_S = 4$. Figure 6.18a shows the validation loss of CNN_{RF} against the number of noisy channel realizations L . We observe that the loss is satisfactory for $L \geq 150$; in the simulations, we keep $L = 200$. Note that this is a common result for different number of channel realizations N . In fact, we use $N = 100$ to achieve reasonable network accuracy. To investigate the performance of deep networks against different noise levels in the training data, we demonstrate the validation loss of CNN_{RF} and the classification accuracy of CNN_{AS} in Fig. 6.18b for different N_{RS} values. It is clear here that both networks attain satisfactory network accuracy for $\text{SNR}_{\text{TEST}} \geq 0\text{dB}$. At low SNR regimes, CNN has poor classification performance due to the deviations between the input and the channel matrices used in the training data. In order to make CNN more robust to noisy inputs, we draw the training data for multiple $\text{SNR}_{\text{TRAIN}}$ levels. Nevertheless, noise in the training data expectedly limits the performance since the network cannot distinguish the input data if it is corrupted too much.

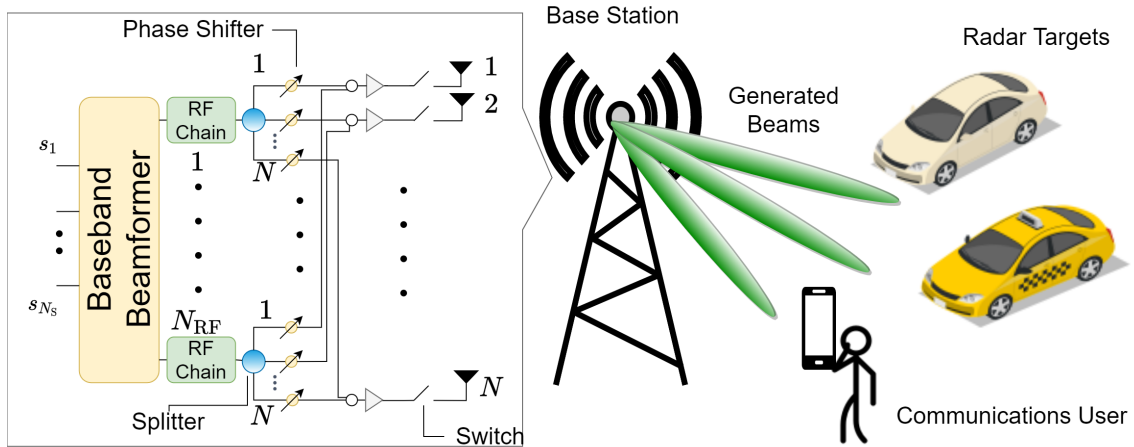


Figure 6.19: ISAC hybrid beamforming scenario with antenna selection.

This issue is also reported in [46, 96] for the multiple $\text{SNR}_{\text{TRAIN}}$ case.

The channel statistics are important parameters that change in very short time in mm-Wave channels. Hence, in the training stage, we feed the network with channel realizations of different N_c values. To further investigate the performance with respect to different channel statistics, we compare the algorithms in Fig. 6.18c and d for different N_c and σ_{Θ}^2 , respectively. The CNN framework provides robust performance against different channel statistics. The effectiveness of the DL techniques can be attributed to training the network with several channel statistics and adding synthetic noise for multiple $\text{SNR}_{\text{TRAIN}}$ values.

As a result, the DL network provides robust performance against the changes in channel statistics without a need to be re-trained. However, when there is a change in the *full array* system parameters such as N_T , N_R , N_{RS} and N_S , the network does need to be re-trained because these parameters directly dictates the dimensions of the network input and output layers.

6.7. Deep Sparse Arrays for ISAC

To jointly access and manage the limited electromagnetic spectrum, ISAC has been envisaged as a technology that will use the same transmit/receive hardware for both radar and communications [54, 97]. In ISAC (Fig. 6.19), the aim is to select the subarray that provides both the best radar sensing and communications performance. In particular, we design the hybrid beamformers corresponding to the selected subarray while maximizing the beamforming performance toward both radar targets and communications users. Due to the combinatorial nature of the antenna selection problem, the computational complexity of the joint (antenna selection and beamforming) problem is high. To combat this challenging problem, a low-complexity approach is devised, wherein the consecutive antennas in the whole array are partitioned into small groups so that the number of possible subarray configurations can be reduced. Then, we introduce an optimization problem to

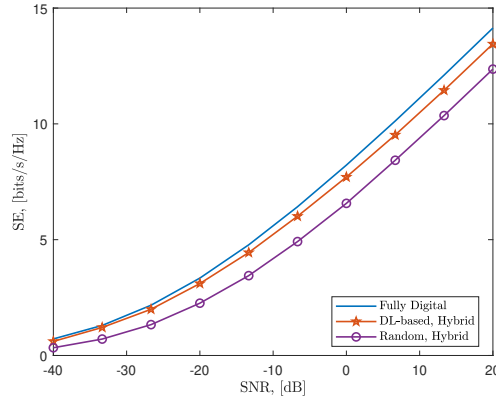


Figure 6.20: ISAC hybrid beamforming performance with antenna selection.

jointly select the *best* subarray and design the hybrid analog and digital beamformers for the ISAC scenario. Finally, a DL-based approach is proposed to further lower the computational burden of the design problem. In particular, a CNN is devised such that the input of the CNN is the combination of both communications (channel matrix) and sensing (radar-only beamformer) related data. The output of the learning model is the combination of the digital beamformer and the sparse analog beamformer.

Fig. 6.20 shows the spectral efficiency (SE) of the joint antenna selection and beamformer design in the ISAC scenario. DL-based CNN achieves a performance very close to the fully digital ISAC beamformer [97], which is computed in accordance with the selected sparse array by the CNN. In comparison, the random selection has a poorer SE.

6.8. Summary

In this chapter, we reviewed DL-based sparse array design principles, procedures, and applications with a focus on direction finding. In general, this problem may be viewed as either a classification or regression in the DL framework. Our DL-based design offers the advantages of feature engineering and prediction-stage computational efficiency. This is particularly useful for dynamic sparse array design scenarios such as in cognitive radar, where a new sparse array must be selected to adapt to the changes in the target environment. Here, we employed a CNN to find the antenna subarray that yields the minimum CRB of the DoA estimation error. Further, antenna selection knowledge already learned at a pre-trained model may be used for a different antenna array geometry using TL methods. This has applications in metacognitive radars [98]. For 2-D or planar sparse arrays, we illustrated the use of SA-assisted DL algorithms. There are a large number of deep sparse array applications in wireless communications, wherein antenna selection is generally employed to reduce the complexity of common functions such as beamforming, channel estimation, and ISAC.

There are many interesting open challenges that need to be tackled for practical

and futuristic implementations of DL-based sparse array techniques. Training a learning model still requires solving complex optimization problems for each training data sample offline prior to training. For instance, the learning models are pivoted by a reasonable trade-off between an efficient implementation and satisfactory beampattern (radar sensing) and spectral efficiency (communications) performance. Practical implementations may employ compressed or quantized model parameters to reduce model complexity. Further, data/model parallelization is useful for accelerating training times.

Bibliography

- [1] Elbir AM, Mishra KV, Vorobyov SA, Heath Robert W Jr. Twenty-five years of advances in beamforming: From convex and nonconvex optimization to learning techniques. *IEEE Signal Processing Magazine*. 2023;40(4):118-31.
- [2] Shenoy RP. Phased array antennas. In: Galati G, editor. *Advanced radar techniques and systems*. Peter Peregrinus; 1993. p. 598-821.
- [3] Frank J, Richards JD. Phased array radar antennas. In: Skolnik MI, editor. *Radar handbook*. 3rd ed. McGraw-Hill Education; 2008. p. 13.1-13.74.
- [4] Herd JS, Conway MD. The evolution to modern phased array architectures. *Proceedings of the IEEE*. 2015;104(3):519-29.
- [5] Haupt RL. *Timed arrays: Wideband and time varying antenna arrays*. John Wiley & Sons; 2015.
- [6] Johnson DH. The application of spectral estimation methods to bearing estimation problems. *Proceedings of the IEEE*. 1982;70(9):1018-28.
- [7] Linebarger DA, Sudborough IH, Tollis IG. Difference bases and sparse sensor arrays. *IEEE Transactions on Information Theory*. 1993;39(2):716-21.
- [8] Haupt RL. Thinned arrays using genetic algorithms. *IEEE Transactions on Antennas and Propagation*. 1994;42(7):993-9.
- [9] Mishra KV, Kahane I, Kaufmann A, Eldar YC. High spatial resolution radar using thinned arrays. In: *IEEE Radar Conference*; 2017. p. 1119-24.
- [10] Lo YT. A mathematical theory of antenna arrays with randomly spaced elements. *IEEE Transactions on Antennas and Propagation*. 1964;12(3):257-68.
- [11] Agrawal VD, Lo YT. Mutual coupling in phased arrays of randomly spaced antennas. *IEEE Transactions on Antennas and Propagation*. 1972;20(3):288-95.
- [12] Wang X, Chen Z, Ren S, Cao S. DOA estimation based on the difference and sum coarray for coprime arrays. *Digital Signal Processing*. 2017;69:22-31.
- [13] Sedighi S, Bhavani Shankar MR, Mishra KV, Ottersten B. Optimum design for sparse FDA-MIMO automotive radar. In: *Asilomar Conference on Signals, Systems, and Computers*; 2019. p. 913-8.
- [14] Lv W, Mishra KV, Chen S. Co-Pulsing FDA Radar. *IEEE Transactions on Aerospace and Electronic Systems*. 2023;59(2):1107-26.

- [15] BouDaher E, Ahmad F, Amin MG, Hoorfar A. Mutual coupling effect and compensation in non-uniform arrays for direction-of-arrival estimation. *Digital Signal Processing*. 2017;61:3-14.
- [16] Liu CL, Vaidyanathan PP. Super nested arrays: Linear sparse arrays with reduced mutual coupling; Part I: Fundamentals. *IEEE Transactions on Signal Processing*. 2016;64(15):3997-4012.
- [17] Liu CL, Vaidyanathan PP. Hourglass arrays and other novel 2-D sparse arrays with reduced mutual coupling. *IEEE Transactions on Signal Processing*. 2017;65(13):3369-83.
- [18] Elbir AM, Mishra KV. Joint antenna selection and hybrid beamformer design using unquantized and quantized deep learning networks. *IEEE Transactions on Wireless Communications*. 2020;19(3):1677-88.
- [19] Foucart S, Rauhut H. *A Mathematical Introduction to Compressive Sensing*. Birkhäuser; 2013.
- [20] Unz H. Nonuniform arrays with spacings larger than one wavelength. *IRE Transactions on Antennas and Propagation*. 1962;10(5):647-8.
- [21] Ishimaru A, Chen YS. Thinning and broadbanding antenna arrays by unequal spacings. *IEEE Transactions on Antennas and Propagation*. 1965;AP-13(1):34-42.
- [22] Sandler SS. Some equivalences between equally and unequally spaced arrays. *IRE Transactions on Antennas and Propagation*. 1960;8(5):496-500.
- [23] Skolnik MI, Nemhauser G, Sherman JW. Dynamic programming applied to unequally spaced arrays. *IEEE Transactions on Antennas and Propagation*. 1964;12(1):35-43.
- [24] Redlich RW. Iterative least-squares synthesis of nonuniformly spaced linear arrays. *IEEE Transactions on Antennas and Propagation*. 1973;21(1):106-8.
- [25] Schjær-Jacobsen H, Madsen K. Synthesis of nonuniformly spaced arrays using a general nonlinear minimax optimisation method. *IEEE Transactions on Antennas and Propagation*. 1976;24(4):501-6.
- [26] Murino V, Trucco A, Regazzoni CS. Synthesis of unequally spaced arrays by simulated annealing. *IEEE Transactions on Signal Processing*. 1996;44(1):119-23.
- [27] Haupt RL. *Antenna arrays: A computational approach*. Wiley-IEEE Press; 2010.
- [28] Kim Y, Jaggard DL. The fractal random array. *Proceedings of the IEEE*. 1986;74(9):1278-80.
- [29] Lo YT, Lee SW. A study of space-tapered arrays. *IEEE Transactions on Antennas and Propagation*. 1966;14(1):22-30.

- [30] Willey R. Space tapering of linear and planar arrays. *IRE Transactions on Antennas and Propagation*. 1962;10(4):369-77.
- [31] Moffet A. Minimum-redundancy linear arrays. *IEEE Transactions on Antennas and Propagation*. 1968;16(2):172-5.
- [32] Arzac J, Danjon A. Nouveau réseau pour l'observation radio astronomique de brillance sur le soleil à 9359 MC. *Comptes Rendus Hebdomadaires Des Seances De L Academie Des Sciences*. 1955;240(9):942-5. In French.
- [33] Camps A, Cardama A, Infantes D. Synthesis of large low-redundancy linear arrays. *IEEE Transactions on Antennas and Propagation*. 2001;49(12):1881-3.
- [34] Bracewell RN. Optimum spacings for radio telescopes with unfilled apertures. In: *URSI Assembly*; 1966. p. 243.
- [35] Leech J. On the representation of $1, 2, \dots, n$ by differences. *Journal of the London Mathematical Society*. 1956;1(2):160-9.
- [36] Schwartau F, Schröder Y, Wolf L, Schoebel J. Large Minimum Redundancy Linear Arrays: Systematic Search of Perfect and Optimal Rulers Exploiting Parallel Processing. *IEEE Open Journal of Antennas and Propagation*. 2021;2:79-85.
- [37] Ishiguro M. Minimum redundancy linear arrays for a large number of antennas. *Radio Science*. 1980;15(6):1163-70.
- [38] Vaidyanathan PP, Pal P. Sparse sensing with co-prime samplers and arrays. *IEEE Transactions on Signal Processing*. 2010;59(2):573-86.
- [39] Qin S, Zhang YD, Amin MG. Generalized coprime array configurations for direction-of-arrival estimation. *IEEE Transactions on Signal Processing*. 2015;63(6):1377-90.
- [40] Zheng W, Zhang X, Li J, Shi J. Extensions of co-prime array for improved DOA estimation with hole filling strategy. *IEEE Sensors Journal*. 2021;21(5):6724-32.
- [41] Kozick RJ, Kassam SA. Linear imaging with sensor arrays on convex polygonal boundaries. *IEEE Transactions on Systems, Man, and Cybernetics*. 1991;21(5):1155-66.
- [42] Duman TM, Ghayeb A. Antenna selection for MIMO systems. In: *Coding for MIMO communication systems*. John Wiley & Sons; 2007. p. 287-315.
- [43] Joshi S, Boyd S. Sensor selection via convex optimization. *IEEE Transactions on Signal Processing*. 2009;57(2):451-62.
- [44] Godrich H, Petropulu AP, Poor HV. Sensor selection in distributed multiple-radar architectures for localization: A knapsack problem formulation. *IEEE Transactions on Signal Processing*. 2012;60(1):247-60.

- [45] Elbir AM, Mishra KV. Robust hybrid beamforming with quantized deep neural networks. In: IEEE International Workshop on Machine Learning for Signal Processing; 2019. p. 1-6.
- [46] Elbir AM, Mishra KV, Eldar YC. Cognitive radar antenna selection via deep learning. IET Radar, Sonar & Navigation. 2019;13:871-80.
- [47] Yu D, Deng L. Deep learning and its applications to signal and information processing [Exploratory DSP]. IEEE Signal Processing Magazine. 2011;28(1):145-54.
- [48] Elbir AM, Mishra KV. Deep learning design for joint antenna selection and hybrid beamforming in massive MIMO. In: IEEE International Symposium on Antennas and Propagation and USNC-URSI Radio Science Meeting; 2019. p. 1585-6.
- [49] Lecun Y, Bengio Y, Hinton G. Deep learning. Nature. 2015;521(7553):436-44.
- [50] Bengio Y, Courville A, Vincent P. Representation learning: A review and new perspectives. IEEE Transactions on Pattern Analysis and Machine Intelligence. 2013;35(8):1798-828.
- [51] Gao Y, Hu D, Chen Y, Ma Y. Gridless 1-b DOA estimation exploiting SVM approach. IEEE Communications Letters. 2017;21(10):2210-3.
- [52] Elbir AM. DeepMUSIC: Multiple signal classification via deep learning. IEEE Sensors Letters. 2020;4(4):1-4.
- [53] Kulkarni P, Vaidyanathan PP. Feature engineering for DOA estimation using a convolutional neural network, for sparse arrays. In: Asilomar Conference on Signals, Systems, and Computers; 2021. p. 246-50.
- [54] Mishra KV, Bhavani Shankar MR, Koivunen V, Ottersten B, Vorobyov SA. Toward Millimeter Wave Joint Radar-Communications: A Signal Processing Perspective. IEEE Signal Processing Magazine. 2019;36(5):100-14.
- [55] Demir ÖT, Tuncer TE. Antenna selection and hybrid beamforming for simultaneous wireless information and power transfer in multi-group multicasting systems. IEEE Transactions on Wireless Communications. 2016;15(10):6948-62.
- [56] Pal P, Vaidyanathan PP. Nested arrays: A novel approach to array processing with enhanced degrees of freedom. IEEE Transactions on Signal Processing. 2010;58(8):4167-81.
- [57] Qin S, Zhang YD, Amin MG. Generalized coprime array configurations for direction-of-arrival estimation. IEEE Transactions on Signal Processing. 2015;63(6):1377-90.
- [58] O'Shea T, Hoydis J. An introduction to deep learning for the physical layer. IEEE Transactions on Cognitive Communications and Networking. 2017;3(4):563-75.

- [59] Wandale S, Ichige K. Design of sparse arrays via deep learning for enhanced DOA estimation. *EURASIP Journal on Advances in Signal Processing*. 2021;2021(1):17-3.
- [60] Aboutanios E, Nosrati H, Wang X. Online antenna selection for enhanced DOA estimation. In: *IEEE International Conference on Acoustics, Speech and Signal Processing*; 2021. p. 8468-72.
- [61] Elbir AM, Mulleti S, Cohen R, Fu R, Eldar YC. Deep-sparse array cognitive radar. In: *IEEE International Conference on Sampling Theory and Applications*; 2019. p. 1-5.
- [62] Pavel SR, Chowdhury Md WTS, Zhang YD, Shen D, Chen G. Machine learning-based direction-of-arrival estimation exploiting distributed sparse arrays. In: *Asilomar Conference on Signals, Systems, and Computers*; 2021. p. 241-5.
- [63] Akter R, Doan VS, Huynh-The T, Kim DS. RFDOA-Net: An efficient ConvNet for RF-based DOA estimation in UAV surveillance systems. *IEEE Transactions on Vehicular Technology*. 2021;70(11):12209-14.
- [64] Gohil RP, Routray G, Hegde RM. Learning based method for robust DOA estimation using co-prime circular conformal microphone array. In: *National Conference on Communications*; 2021. p. 1-6.
- [65] Roy V, Chepuri SP, Leus G. Sparsity-enforcing sensor selection for DOA estimation. In: *IEEE International Workshop on Computational Advances in Multi-Sensor Adaptive Processing*; 2013. p. 340-3.
- [66] Renaux A, Forster P, Larzabal P, Richmond CD, Nehorai A. A fresh look at the Bayesian bounds of the Weiss-Weinstein family. *IEEE Transactions on Signal Processing*. 2008;56(11):5334-52.
- [67] Tabrikian J, Isaacs O, Bilik I. Cognitive antenna selection for DOA estimation in automotive radar. In: *IEEE Radar Conference*; 2016. p. 1-5.
- [68] Isaacs O, Tabrikian J, Bilik I. Cognitive antenna selection for optimal source localization. In: *IEEE International Workshop on Computational Advances in Multi-Sensor Adaptive Processing*; 2015. p. 341-4.
- [69] Stoica P, Nehorai A. MUSIC, maximum likelihood, and Cramér-Rao bound: Further results and comparisons. *IEEE Transactions on Acoustics, Speech, and Signal Processing*. 1990;38(12):2140-50.
- [70] Friedlander B, Weiss AJ. Direction finding in the presence of mutual coupling. *IEEE Transactions on Antennas and Propagation*. 1991;39(3):273-84.
- [71] Nion D, Sidiropoulos ND. Tensor algebra and multidimensional harmonic retrieval in signal processing for MIMO radar. *IEEE Transactions on Signal Processing*. 2010;58(11):5693-705.

- [72] Elbir AM, Mishra KV. Sparse Array Selection Across Arbitrary Sensor Geometries With Deep Transfer Learning. *IEEE Trans Cognit Commun Networking*. 2020 Jun;7(1):255-64.
- [73] Ye Z, Liu C. 2-D DOA estimation in the presence of mutual coupling. *IEEE Transactions on Antennas and Propagation*. 2008;56(10):3150-8.
- [74] Cheng J, Wu J, Leng C, Wang Y, Hu Q. Quantized CNN: A unified approach to accelerate and compress convolutional networks. *IEEE Transactions on Neural Networks and Learning Systems*. 2018;29(10):4730-43.
- [75] Dudgeon DE. Fundamentals of digital array processing. *Proceedings of the IEEE*. 1977;65(6):898-904.
- [76] Athley F. Optimization of element positions for direction finding with sparse arrays. In: *IEEE Signal Processing Workshop on Statistical Signal Processing*; 2001. p. 516-9.
- [77] Duan L, Tsang IW, Xu D. Domain transfer multiple kernel learning. *IEEE Transactions on Pattern Analysis and Machine Intelligence*. 2012;34(3):465-79.
- [78] Kulis B, Saenko K, Darrell T. What you saw is not what you get: Domain adaptation using asymmetric kernel transforms. In: *IEEE Conference on Computer Vision and Pattern Recognition*; 2011. p. 1785-92.
- [79] Pan SJ, Yang Q, et al. A survey on transfer learning. *IEEE Transactions on Knowledge and Data Engineering*. 2010;22(10):1345-59.
- [80] Vincent P, Larochelle H, Lajoie I, Bengio Y, Manzagol PA. Stacked denoising autoencoders: Learning useful representations in a deep network with a local denoising criterion. *Journal of Machine Learning Research*. 2010;11(Dec):3371-408.
- [81] Seyfioğlu MS, Gürbüz SZ. Deep neural network initialization methods for micro-Doppler classification with low training sample support. *IEEE Geoscience and Remote Sensing Letters*. 2017;14(12):2462-6.
- [82] Chen B, Zhong Z, Ai B, Chen X. Comparison of antenna arrays for MIMO system in high speed mobile scenarios. In: *IEEE Vehicular Technology Conference - Spring*; 2011. p. 1-5.
- [83] Hyberg P, Jansson M, Ottersten B. Array interpolation and bias reduction. *IEEE Transactions on Signal Processing*. 2004;52(10):2711-20.
- [84] Rubsamen M, Gershman AB. Direction-of-arrival estimation for nonuniform sensor arrays: From manifold separation to Fourier domain MUSIC methods. *IEEE Transactions on Signal Processing*. 2008;57(2):588-99.
- [85] Liu Y, Chen H, Peng Z, Fang J. DOA estimation for mixed circular and noncircular signals by using the conversion relationship between URAs and a virtual ULA. *IEEE Sensors Letters*. 2019;3(11):1-4.

- [86] Pan SJ, Tsang IW, Kwok JT, Yang Q. Domain adaptation via transfer component analysis. *IEEE Transactions on Neural Networks*. 2010;22(2):199-210.
- [87] Yosinski J, Clune J, Bengio Y, Lipson H. How transferable are features in deep neural networks? In: *Advances in Neural Information Processing Systems*; 2014. p. 3320-8.
- [88] Schmidt RO. Multiple emitter location and signal parameter estimation. *IEEE Transactions on Antennas and Propagation*. 1986;34(3):276-80.
- [89] Nakamura S, Iwazaki S, Ichige K. Optimization and hole interpolation of 2-D sparse arrays for accurate direction-of-arrival estimation. *IEICE Transactions on Communications*. 2021;104(4):401-9.
- [90] Wandale S, Ichige K. 2D sparse array selection via deep learning. In: *International Symposium on Antennas and Propagation*; 2021. p. 445-6.
- [91] Wandale S, Ichige K. Simulated annealing assisted sparse array selection utilizing deep learning. *IEEE Access*. 2021;9:156907-14.
- [92] Nakamura S, Iwazaki S, Ichige K. Optimum 2D sparse array and its interpolation via nuclear norm minimization. In: *IEEE International Symposium on Circuits and Systems*; 2019. p. 1-5.
- [93] Elbir AM, Mishra KV. Deep learning design for joint antenna selection and hybrid beamforming in massive MIMO. In: *IEEE International Symposium on Antennas and Propagation USNC/URSI National Radio Science Meeting*; 2019. p. 1-2.
- [94] Boumal N, Mishra B, Absil PA, Sepulchre R. Manopt, a Matlab toolbox for optimization on manifolds. *Journal of Machine Learning Research*. 2014;15:1455-9.
- [95] Yu X, Shen J, Zhang J, Letaief KB. Alternating minimization algorithms for hybrid precoding in millimeter wave MIMO systems. *IEEE Journal of Selected Topics in Signal Processing*. 2016;10(3):485-500.
- [96] Elbir AM. CNN-based precoder and combiner design in mmWave MIMO systems. *IEEE Communications Letters*. 2019;23(7):1240-3.
- [97] Elbir AM, Mishra KV, Chatzinotas S. Terahertz-band joint ultra-massive MIMO radar-communications: Model-based and model-free hybrid beamforming. *IEEE Journal of Selected Topics in Signal Processing*. 2021;15(6):1468-83.
- [98] Mishra KV, Shankar MB, Ottersten B. Toward metacognitive radars: Concept and applications. In: *IEEE International Radar Conference*; 2020. p. 77-82.